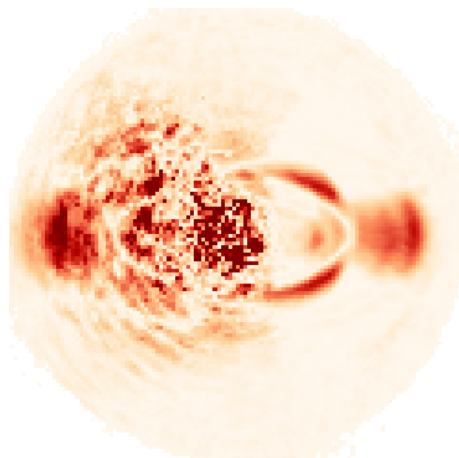


DETECTING DISKS WITH THE VAPP

DAVID KLEINGELD



Astronomy
Faculty of Science
Leiden University

Juni 2019 –

David Kleingeld: *Detecting disks with the vAPP*, , © Juni 2019

SUPERVISORS:

Christoph Keller

Steven Bos

Jos de Boer

LOCATION:

Leiden

TIME FRAME:

Juni 2019

ABSTRACT

A major topic in astronomy is the discovery of exoplanets. Little is known about their formation as it is hard to image the disks they form in. Special instruments and techniques have been developed to image faint objects close to star. Here we see if we can use the vector Apodizing Phase Plate (vAPP) instrument to observe disks and if the Angular Differential Imaging (ADI) technique can improve the results. We simulate disk observations for different disks using a simple disk model and simulated point spread functions (PSFs). Then we apply ADI to the observations.

Properly oriented disks can be observed with the vAPP. When we compare the observations before and after ADI we see the disks shape is distorted by ADI. Disks with features very close to the star at a few λ/D are easier to characterize as ADI concentrates the disks light to the semi major axis. Further study of the vAPP for observing disks is required. We do not recommend looking further at ADI until alternatives such as Reference star Differential Imaging (RDI) have been explored.

CONTENTS

1	INTRODUCTION	1
2	THEORY	5
2.1	Point spread function	5
2.1.1	Atmosphere	7
2.1.2	Adaptive Optics	7
2.2	Vector Apodizing Phase Plate	8
2.3	Disks	9
2.3.1	Categorization and features	9
2.4	Angular differential Imaging	10
3	DATA GENERATION	13
3.1	Disk model	13
3.2	Atmospheric Distortions	14
3.3	Generating observations	15
4	DATA REDUCTION	19
4.1	Pre-Processing	19
4.2	Angular differential imaging	19
4.2.1	Algorithm	19
4.2.2	Control	20
4.3	Parameter Study	21
5	RESULTS	23
6	DISCUSSION AND CONCLUSION	33
6.1	ADI disk results in depth	33
6.2	ADI for dim disks	33
6.3	Characterizing parameters in ADI results	34
6.4	Conclusion	35
7	FUTURE WORK	37
	BIBLIOGRAPHY	39
	APPENDIX	41
7.1	Fourier method	41
7.2	Left coronagraphic PSFs	43
7.3	Right coronagraphic PSFs	50

LIST OF FIGURES

Figure 1	Optical layout of a Lyot coronagraph, by Matthew Kenworthy, from https://home.strw.leidenuniv.nl/kenworthy/app	1
Figure 2	The point spread function (PSF) is the image an instrument produces when looking at a point source such as a star. Here we see the PSF of a instrument without a coronagraph, with the classical Lyot coronagraph and a one using the vector Apodizing Phase Plate (vAPP).	2
Figure 3	Fraunhofer diffraction from an arbitrary aperture, r and R large compared to the size of the hole. Extracted from Optics 5th edition, by [5].	6
Figure 4	Sketch showing the basic principle of an Adaptive Optics (AO) system, adapted from UC Berkeley science review: Into focus, Credit: Keith Cheveralls.	8
Figure 5	Sketch summarizing the different classifications of protoplanetary disks proposed in [3].	10
Figure 6	An overview of Angular Differential Imaging (ADI) for detecting exoplanets, the exoplanet location is indicated with a red dot. From the leftmost column to the right: the input images with field rotation, the median of the input, the input with median subtracted from it, the median subtracted input de-rotated and finally the median of the last step. The rightmost column gives the result of ADI. Credit: M. Kenworthy.	11
Figure 8	Two disks created by the model with different rings and inclination both with a position angle of 45 degrees.	14

Figure 9	Differences between the first PSF of an observation and later PSFs. Compared between simulated observations on the left and on-sky data on the right. The PSFs were aligned then normalized on the maximum of the leakage term, finally the absolute value of the difference between the first and n-th PSF was taken. The second, 10th and 50th simulated PSF are 0.7, 7 and 14 seconds apart in simulation time. These give similar morphology to the on sky differences that are 0.0014, 0.014 and 0.07 seconds apart.	17
Figure 10	A simulated image after the Pre-processing process, first it was aligned and then its right and left coronagraphic PSF were extracted.	20
Figure 11	The right and left end result of ADI applied to a generated image stack of a star. The stack contains 20 images, the field rotation over the entire stack is 60°. Note how de-rotating the fields leads to a circular result as we lose the angles.	21
Figure 12	A detailed look at a disk with one rings. On the top row: the PSF and the disk model used to generate the other images. Then generated images of the disk model en its <i>starless</i> variant (left) and results of ADI applied to them (right).	25
Figure 13	A detailed look at a disk with two rings. On the top row: the PSF and the disk model used to generate the other images. Then generated images of the disk model en its <i>starless</i> variant (left) and results of ADI applied to them (right).	26
Figure 14	The standard disk model, the image it generates and the result after ADI. The model in the right column has half the contrast between the star and the disk as the left one.	27
Figure 15	Comparing a disk with two rings with one that has only one ring. Both columns from top to bottom: the disk, ADI applied to a simulated image of only disk and not the star, ADI applied to a simulated image of the disk and star.	28
Figure 16	Comparing a large and small disk. Both columns from top to bottom: the disk, ADI applied to a simulated image of only disk and not the star, ADI applied to a simulated image of the disk and star.	29

Figure 17	Comparing two disks with different initial field rotation. Both columns from top to bottom: the disk, ADI applied to a simulated image of only disk and not the star, ADI applied to a simulated image of the disk and star.	30
Figure 18	Comparing the standard disk model at 60 and 40 degrees inclination. Both columns from top to bottom: the disk, ADI applied to a simulated image of only disk and not the star, ADI applied to a simulated image of the disk and star.	31
Figure 19	Comparing the extreme of ADI self subtraction at a unrealistic 360 degrees of field rotation to the cause of the self subtraction, the median of the set of images. Both use the vAPP PSF . . .	36
Figure 20	The Pattern used and the differences between PSFs distorted with it using the method described above.	42

ACRONYMS

PSF	point spread function.....	5
vAPP	vector Apodizing Phase Plate	8
APP	Apodizing Phase Plate.....	8
AO	Adaptive Optics	7
HCIPy	high-contrast imaging python	15
ADI	Angular Differential Imaging.....	10

INTRODUCTION

A major and successful topic in astronomy has been the discovery and characterization of exoplanets, planets orbiting another star. This allows us to base planetary physics on data outside our solar system, understand how typical the solar system is and quantify how rare life is. The interest in exoplanets has sparked great progress in the field of high contrast imaging resulting in new imaging techniques and instruments. At the time of writing 3,949 planets have been confirmed.

Large questions still exist around the formation of planets. Certain is that a protoplanetary disk is an important stage in the formation of a planetary system however the exact mechanisms [22] [1] [16] are unknown. These flat disks of dust and gas extend up to hundreds of AU. They generally persist for millions of years. Their exact morphology, especially at small radii is a topic of much debate [12]. The disks can be observed within the visible spectrum, near infrared and radio. Each wavelength probes different molecules materials and processes. ALMA has been successful in mapping emissions from molecules while optical and near infrared map the scattered light from the disk.

To observe a disk in the optical and infrared is however a great challenge due to the high contrast between the disk and its star at the required angular resolution. For ground-based observations adaptive optics are used. This negates most of the atmospheric seeing.

Reducing contrast is done with a coronagraph, an instrument that blocks the light from a star. The classic Lyot coronagraph blocks the star light in the focal-plane (see: Figure 1). In the focus an opaque mask is placed, it scatters the starlight. Then in the pupil-plane a ring shaped mask blocks most of the now scattered star light. Then at the second focus the image is recorded on the detector.

A Lyot coronagraph is not able to observe disks close to stars because it blocks all the light at small separations from the star. The vAPP

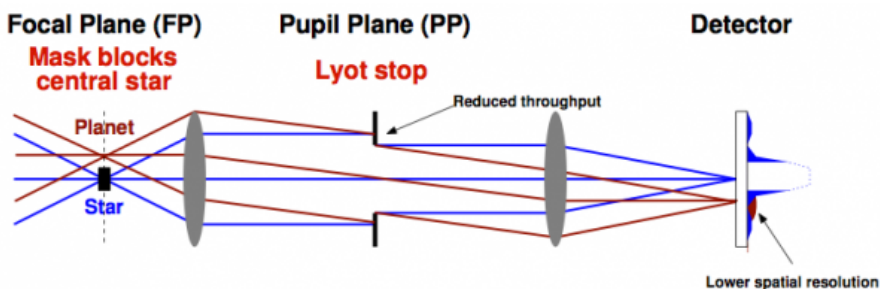


Figure 1: Optical layout of a Lyot coronagraph, by Matthew Kenworthy, from <https://home.strw.leidenuniv.nl/kenworthy/app>

[20] is a type of coronagraph placed at the pupil of a telescope. The vAPP removes the star light close to the star by modifying the phase of incoming light. This phase change flips the light in a D-shaped region around the star to the other side. Any faint object next to the star in the now dark region becomes detectable. Before the vAPP does this it creates two copies, here we call these coronagraphic PSFs, see the red circles in Figure 2d. The two copies of the star. Compared to the classic Lyot coronagraph the vAPP can reduces starlight very close to a star to a greater degree, see Figure 2.

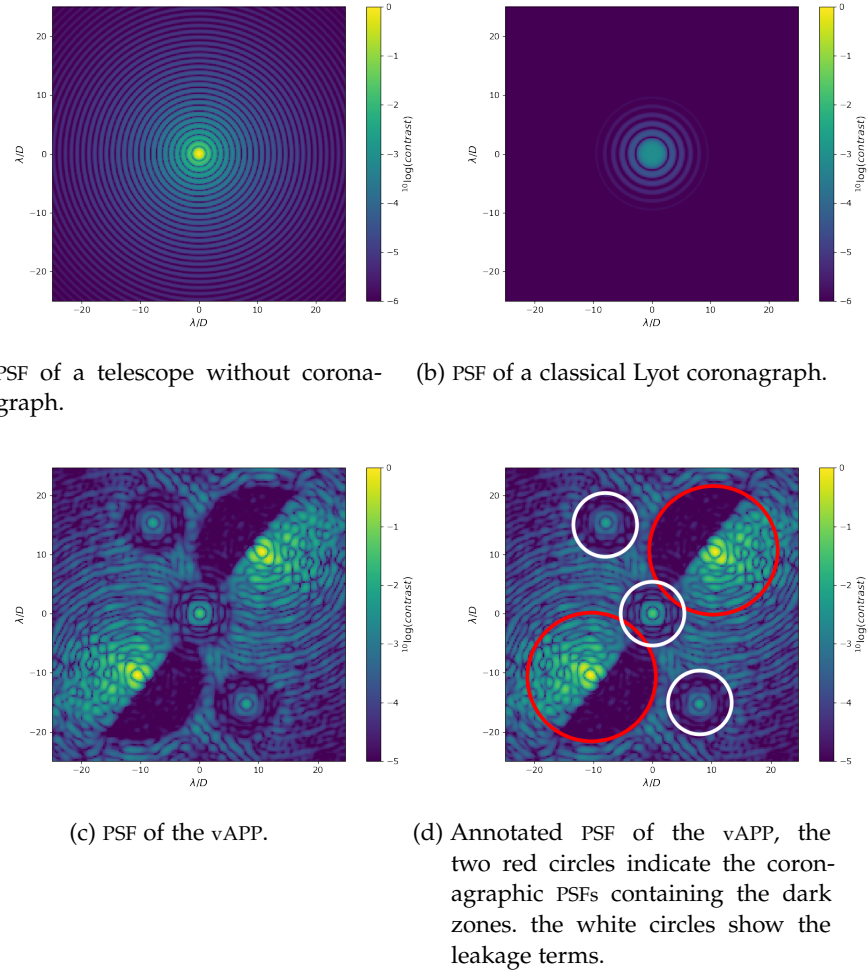


Figure 2: The PSF is the image an instrument produces when looking at a point source such as a star. Here we see the PSF of a instrument without a coronagraph, with the classical Lyot coronagraph and a one using the vAPP.

The vAPP has mainly been developed to detect exoplanets. However it could also allow us to resolve disk features and study disks in greater detail directly. However as the vAPP has a peculiar PSF (ee Figure 2c and the entire disk will never lie within one of the dark

zones it might proof challenging to differentiate disk features from the PSFs features.

ADI is a technique to remove stationary and slowly changing PSF structures from an image. It does so by rotating the field of view while keeping the PSF still. It has been well proven for the detection of companions such as exoplanets however it suffers from self subtraction when applied to disks [15] [18]. ADI removes rotational symmetry, therefore it might create large scale distortions in the result.

Here we see if we can use the vAPP instrument to observe disks and if the ADI technique can improve the results. We simulate disk observations for different disks using a simple disk model and simulated PSFs. Then we apply ADI to the observations.

We begin with an overview of the theory behind simulating observations, disks and ADI. Then we focus on how we have generated the observations. This is followed by a chapter detailing data reduction and then the results are shown, detailing the disks, simulated observations and how they change after data reduction. Finally we discuss the results and give our conclusion.

2

THEORY

Here we discuss what an point spread function (PSF) is, how it helps us describe an optical system and how they naturally appear from basic optics. Then we look at the different types of disks that have been observed and what contrasts we expect.

2.1 POINT SPREAD FUNCTION

We can describe what happens to light going through an optical system with its PSF. It describes the light intensity on the focal-plane (where the science detector is) as a function of x and y when a single point source is imaged on the center of the focal-plane.

Light is an propagating electromagnetic wave. We derive how to find the PSF from the Huygens-Fresnel Principle. It states that any part of a wave can be described as a front of infinitely many point sources interfering with one another. An optical element can change these arrangement of theses sources, for example an aperture allows only a small area to be filled with these point sources as illustrated in [Figure 3](#).

We find the electric field at a point P at distance R by summing up the fields of these infinite point sources taking into account the different distances to R . Writing the infinite sum as an integral we get [Equation 1a](#) for the electric field at a point P some distance R from an aperture.

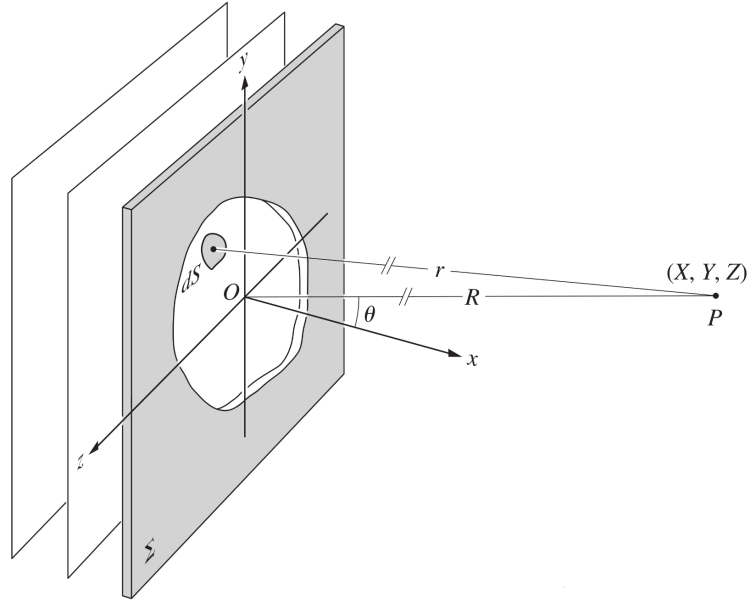
$$E = \frac{\varepsilon_A e^{i(wt - kR)}}{R} \iint_{\text{Aperture}} e^{ik(Yy + Zz)/R} dy dz \quad (1a)$$

Here Y, Z describe the position in the imaging plane in which P lies as seen in [Figure 3](#). Small letters y and z are the position in the aperture plane. The integral is over the aperture, only integrating over the transparent parts.

Here we integrate only over the aperture and assume all light is transmitted within and no light outside of it. To allow for changes in phase and magnitude caused by for example dirty glass, or a complicated optical instrument don not integrate over only an aperture but use an aperture function and integrate over all space.

$$\mathcal{A}(y, z) = \mathcal{A}_0(y, z) e^{i\phi(y, z)} \quad (2)$$

Figure 3: Fraunhofer diffraction from an arbitrary aperture, r and R large compared to the size of the hole. Extracted from Optics 5th edition, by [5].



Here the time changing electromagnetic wave ϵ is averaged into a constant field of magnitude one. Then the transmission through the aperture changes the magnitude (\mathcal{A}) and the phase ($\phi(y, z)$).

$$E(Y, Z) = \iint_{-\infty}^{\infty} \mathcal{A}(y, z) e^{ik(Yy + Zz)/R} dy dz \quad (1b)$$

The expression for the E field at the point P (Equation 1a) rewritten to make use of the aperture function.

We can rewrite this to get rid of the dependence on the distance by substituting $K_y = kY/R$ and $K_z = kZ/R$ for Y and Z . This gives the final form:

$$E(K_Y, K_Z) = \iint_{-\infty}^{\infty} \mathcal{A}(y, z) e^{i(K_Y y + K_Z z)} dy dz \quad (1c)$$

This is the 2 dimensional Fourier transformation of the aperture function. Thus “the field distribution in the Fraunhofer diffraction pattern is the Fourier transform of the field distribution across the aperture (i.e. the aperture function)” [5]. Here the Fraunhofer diffraction pattern is the instruments focal-plane.

For the PSF we are interested in the intensity which is not the electric field E but $|E|^2$. This means we can calculate the PSF of an instrument by Fourier transforming its (complex) aperture function and

squaring the result. Note that the amplitude in the aperture function does not only have to depend on the shape of the aperture as there might be partially transparent material. We can use it to simulate any optical instrument such as the vector Apodizing Phase Plate (vAPP).

With the PSF we know how a single point source would look when imaged by an optical system. If we assume the system is linear system we can use the superposition principle to image extended sources by convolving the PSF with the extended source.

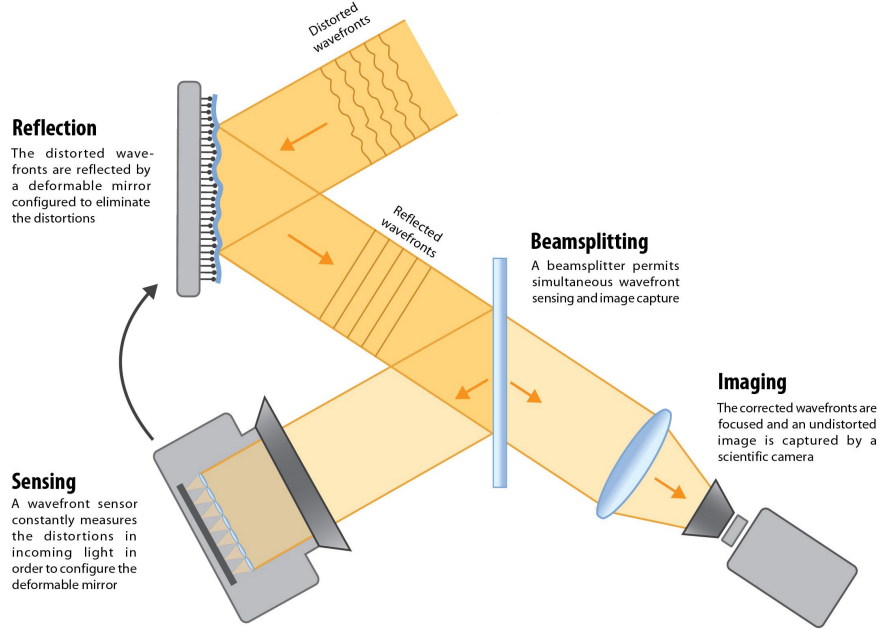
2.1.1 *Atmosphere*

The telescope or coronagraph are not the only optical system at play. There are many differently moving layers of air between the telescope and space. These work as independent optical systems that change in time. The varying temperature and humidity between and within layers changes the air's refractive index resulting in phase changes. Each layer moves in a different direction at a different speed as winds differ between altitudes. Combined this causes the complete PSF to change continuously. The changes are smaller at smaller timescales as the layers move less far and temperature and humidity change less.

2.1.2 *Adaptive Optics*

Since the 1990's Adaptive Optics (AO) are used. They utilize an adaptive mirror that can change its shape to undo the phase changing of the atmosphere, see [Figure 4](#). To do this they first need to measure the errors in the wavefront. However as these measurement are not instant the shape of the mirror can never match the current wavefront. There are also some errors in positioning the mirror will always match the required shape. Both these effects cause small distortions in the final image. Thus even with AO the total PSF for the atmosphere, the AO, the telescope and the instrument will keep changing in time, however the magnitude of the change is severely reduced. Adaptive optics do not correct the entire field. Each system has a control radius around the star in which the AO can reduce the seeing.

Figure 4: Sketch showing the basic principle of an AO system, adapted from UC Berkeley science review: Into focus, Credit: Keith Cheveralls.



2.2 VECTOR APODIZING PHASE PLATE

As mentioned in the introduction, the vector Apodizing Phase Plate (vAPP) is not a conventional coronagraph that blocks light. It is a coronagraph that changes the phase in the pupil-plane to create destructive interference in an area of the PSF. This creates a dark zone in the PSF. Dim objects can be imaged if the contrast between them and the star is smaller than the contrast between center peak of the PSF and the noise in the dark zone. The contrast can be higher if post processing techniques such as Angular Differential Imaging (ADI) are used (see [Section 2.4](#)).

As the coronagraph works in the pupil-plane it is insensitive to the effects of tip tilt errors, which are caused by vibrations in the telescope or imperfectly corrected atmospheric tip tilt effects. Furthermore unresolved stars do not limit how close to a star the coronagraph can function.

The vAPP iterates on the Apodizing Phase Plate (APP), it creates its destructive interference by introducing differences in the optical path length thereby changing the phase. These changes are designed to create the mentioned dark zone in the shape of a 180° half circle with a radius of 2 to 9 λ/D [2]. To achieve these phase changes the path length differences need to change throughout the pupil. The design

is stored as a heightmap of the required path differences. It is then manufactured by diamond turning glass.

Instead of modifying the optical path length, the vAPP introduces the phase changes using the geometrical properties of a liquid crystal plate. The two circular polarization receive opposite phase and create dark holes at opposite sides of the PSF [20] [14] [2]. By then splitting the right and left handed light and imaging both separated we get not 180° of dark zone but 360° solving one of the major problems of the APP. Here we refer to the small PSFs within the full PSF as coronagraphic PSFs, see [Figure 2d in Chapter 1](#).

2.3 DISKS

With the formation of a star it is inevitable a disk will form due to the conservation of angular momentum. While initially material will orbit in various directions and planes these will slowly cancel out due to collisions and attraction leaving the average plane and direction as the final orientation of a disk around the star. It seems likely these disk will allow the formation of planets due to the high detection rate of exoplanets [21].

The formation of disks goes through 3 main stages[21]. Only the last stage allows direct imaging in the near-IR and optical bands though all are observable in Radio:

1. Right after the molecular core collapses, most mass is still in a cloud surrounding the disk and the star. Due to that it is not possible to see the disk in the near-IR or optical regime.
2. Most mass has moved into the star, the disk is partially obstructed by outflow of mass from the star. The enveloping mass is about the same as the disks.
3. Central star becomes visible, the enveloping dust has cleared or accreted onto the disk and the disk only contains a few percent of the total mass of the system. It now is a protoplanetary disk.

During the first two stages the disk is obstructed by dust. These stages take a relatively short time. However at the third stage we should be able to study the disk. During this stage planets can form. Their formation process is uncertain.

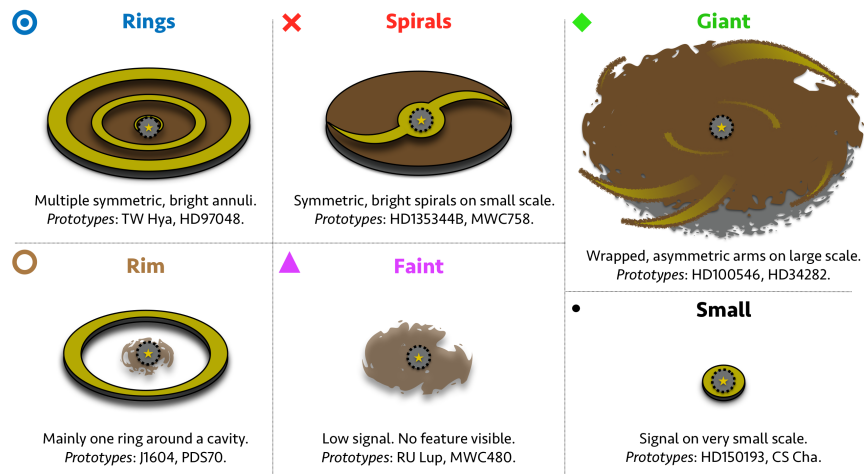
2.3.1 *Categorization and features*

It is suspected the disks features are linked to the formation of planets. Rings in a disk could indicate a planet embedded in the disk [8] however those planets can currently not be detected. There is also evidence that spirals in disks can be caused by planets in the disk [3].

This means the morphology of disks can provide valuable insight in how planets form.

Disks seem to be ring or spiral shaped with some forms in between. They can be classified into 6 categories [3] see [Figure 5](#).

[Figure 5](#): Sketch summarizing the different classifications of protoplanetary disks proposed in [3].



With this categorization which is still topic of much debate they [3] further conclude:

- faint disks are young
- spiral disks are around stars that almost start their main sequence
- ring disk have no outer stellar companion

Furthermore they [3] conclude that in small disks of 10 to 20 Au in size and young faint disks structures remain undetected. Observing disks using the vAPPs which aims to allow imaging at few λ/D could allow us to detect these structures.

2.4 ANGULAR DIFFERENTIAL IMAGING

Angular Differential Imaging (ADI) [9] is a technique to remove stationary and slowly changing PSF structures from an image. It is a proven method for the detection of companions with classic PSFs such as the one in [Figure 2a](#).

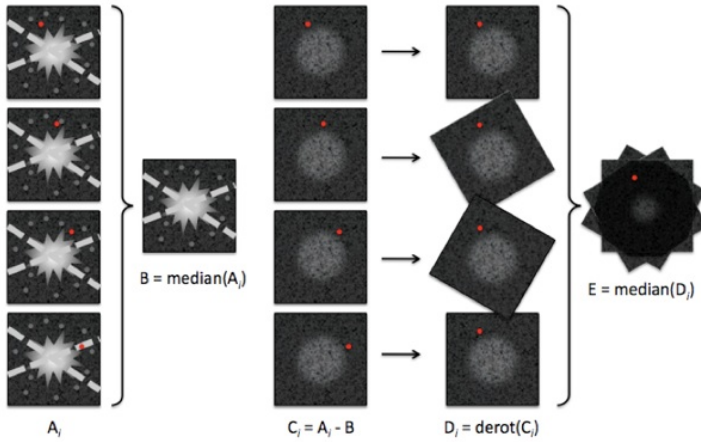


Figure 6: An overview of ADI for detecting exoplanets, the exoplanet location is indicated with a red dot. From the leftmost column to the right: the input images with field rotation, the median of the input, the input with median subtracted from it, the median subtracted input de-rotated and finally the median of the last step. The rightmost column gives the result of ADI. Credit: M. Kenworthy.

ADI is a 4 step process. It is easiest to explain for an exoplanet observed using a normal telescope with symmetrical PSF. We follow the illustration in Figure 6. The input is a collection of noisy images with one hidden exoplanet (indicated by the red dot). The input was made with field rotation enabled, each image is rotated slightly further than previous one. The exoplanet, though indicated, can not be detected in the input and a number of bright noise spots caused by the instrument are present, these naively seem exoplanets. As they are caused by the instrument the bright noise spots do not rotate as the telescopes field does, they are in the same place for every image in the input. To process an image sequence we go through these steps:

1. First we create a median of all the images. The exoplanet appears in the median multiple times however dramatically dimmer while the bright noise spots are at around the same brightness.
2. Now we subtract the median from each of the input images. As the noise spots are about as bright in the median as in the input images they get mostly removed while the exoplanet only drops slightly in brightness as it is much brighter in the input than in the median.
3. Then the input is de-rotated. For each input in the image we make sure the image of the sky lines up by rotating back the rotation that was introduced during observing. The exoplanet is now at the same spot on each image in the sequence while the noise is spread out.

4. Finally we combine the images from the previous step. The light of the exoplanet in all the images gets added up while the noise is spread out and stays around the same level.

To use ADI with the vAPP we make sure the entire rotation fits in one of the two dark holes. This makes post processing easier as we do not need to worry about merging data from the two dark holes.

Applying ADI to disk images might however have adverse effects. For a circular disk the field rotation will change little to the image. The median created in the first step will just be an image of the disk. When we subtract the median from the input the disk will disappear. This is called self subtraction. The less symmetrical a disk is, due to high inclination for example, the less self subtraction we will have.

3

DATA GENERATION

There are no observations of disks with the vAPP. Here we describe how we simulate observations using a disk model and PSFs. This presents a number of advantages though the main reason is the lack of disk observations using the vAPP. Generating the data from a model allows us to vary parameters as we wish. We can try a reduction method on a simple slightly inclined disk or a near face-on disk with many rings. By reducing images with varying disk morphology we can map how a reduction method performs for each disk morphology. Most importantly we can clearly separate artifacts created during data reduction from disk features when we know what the disk looks like.

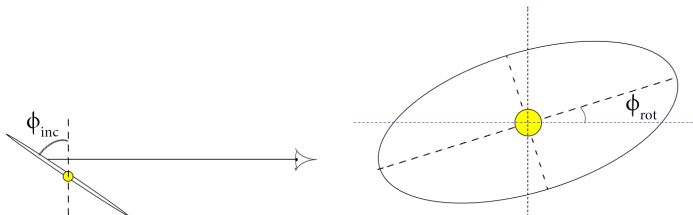
3.1 DISK MODEL

We use a 2-dimensional thin disk model based on the work by [4]. The model has 4 basic parameters:

INCLINATION The angle the disk is tilted towards the observer. A 0 degrees inclination gives a face-on disk and 90 degrees a horizontal line being an edge on disk. As illustrated in [Figure 7b](#)

POSITION ANGLE After inclination the disk can be rotated around the line of sight from the observer, rotation to the left is positive. See [Figure 7a](#)

INNER AND OUTER RADII Disks consist of one or more rings that start and stop at some radius from the star. The inner and outer radius are relative to the size of the image generated and expressed in percent. An Inner radius of 20% gives a hole in the disk with a diameter of 20% of the image width.



(a) Inclination angle from: [4]

(b) Position angle, from: [4]

The disk is modeled as optically thick and does not emit light on its own. At a certain radii between the inner and outer radii (r) the disks brightness profile is given by:

$$B(r) = 1 \cdot \left(\frac{R_{\text{star}}}{r} \right)^2 \quad (3)$$

Here $B(r)$ is the value of a disk pixel at distance r in AU and R_{sun} is the suns radius. The disk pixel values are increased until the required contrast between star and disk is reached. For all disks discussed here except otherwise noted this factor is 50.

We evaluate the model onto an image of 200 by 200 pixels. This speeds up calculations and is similar to the resolution of observed vAPP data-sets. The model behaves well for most disks however on this resolution features that are small in the observers plane are pixelated. We can make disks larger then the full image width if they are inclined and rotated as we see in [Figure 8](#) below..

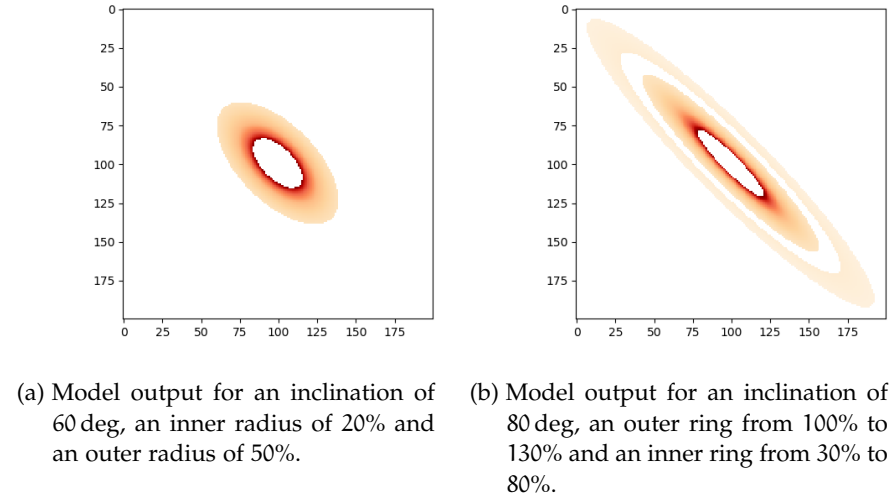


Figure 8: Two disks created by the model with different rings and inclination both with a position angle of 45 degrees.

3.2 ATMOSPHERIC DISTORTIONS

To simulate an observation we do not use a single given PSF. Since during an observation the combined PSF of the atmosphere and instrument changes. However a complete simulation of these effects is outside the scope of the thesis. Instead we try to approach a similar morphology to an on-sky-PSF, with similar changes in time. We add an atmosphere simulation to the PSF generation then compare the result to on-sky observations.

We create the PSFs using high-contrast imaging python (HCIPy), an open-source object-oriented framework written in Python for performing end-to-end simulations of high-contrast imaging instruments [17]. The framework is used to generate PSFs with a very rough simulation. We use the provided methods in HCIPy to create a multi-layer atmospheric model that changes in time. Then we use that model, the vAPP amplitude screen and vAPP phase screen to generate a series of PSFs using:

$$I_{\text{vAPP}} = |\mathcal{F}_{2d}(Ae^{i\theta})|^2 + |\mathcal{F}_{2d}(Ae^{-i\theta})|^2 + |\mathcal{F}_{2d}(A) \cdot C|^2 \quad (4)$$

With I_{vAPP} the vAPP PSF, \mathcal{F}_{2d} the 2 dimensional Fourier transformation. A and $e^{\pm i\theta}$ represent an amplitude and phase change imparted on the light by the vAPP.

Here we use not one aperture function as in [Section 2.1](#) but combine three. The first two ($Ae^{\pm i\theta}$) simulate the opposing phases the circular polarization receive from the vAPP (see [Figure 2d](#)). The third factor, is called the leakage term.

Instead of modeling an adaptive optics system we modified the Fried parameter for the atmosphere to get similar morphological changes in time to the available on-sky images. This is sufficient as the dark hole, where we will observe the disk, will lie in the control radius of the AO which means the effect of an AO system on the disk will mostly be an increase in resolution by reducing the seeing effect.

We use a telescope diameter of 8.2m and a wavelength, of $1 \cdot 10^{-6}$ m for the generation. For a Fried parameter of 4m and exposure time of 0.7 seconds we find quantitatively similar PSF mythologies to the on-sky data¹. To put this into perspective: to simulate excellent seeing conditions we would use a Fried parameter of 20cm. With these settings we use HCIPy to create an ordered set of PSFs changing through time as the simulated atmosphere evolves. See [Figure 9](#) for the difference between the first PSF in a set and later PSFs in the same set, compared between on-sky and simulated PSFs. Note that as time evolves the differences between first and later PSFs grow. The “brightness” of the differences can not be compared as the on sky data saturates the detector for most of the coronagraphic PSF. Qualitatively on-sky and generated PSFs evolve similar in time. We decide to use this method to generate all PSFs.

3.3 GENERATING OBSERVATIONS

To get a data-set that simulates an observation we create an ordered set of disk images each one rotated a bit with respect to the previous

¹ Unpublished data taken with the SCExAO instrument on the Subaru telescope during an engineering night in the summer of 2017.

image. This accounts for the field rotation between images caused by observing with an alt-azimuth telescope in pupil-stabilized mode. The angle depends on the time between images and the field rotation rate.

$$\psi = 0.2506 \cdot \frac{\cos(A) \cos \phi}{\sin(z)} \quad (5)$$

The field rotation ψ in degrees per minute for a given target azimuth A , zenith distance z and telescope latitude ψ [11, page 95]. If we would be observing from Mauna Kea (latitude 19.8) at 30 degrees from the zenith this gives a rotation rate between 0 and 14.74 degrees per minute.

Now to get the simulated observation an ordered set is created by convolving each n-th image from the disk set with the n-th image of the PSF set. These are the simulated observations through time.

Using variations on this method we create 3 different sets.

1. Place the star as a single pixel with value one in the center of the disk before going through the above procedure. This is our observation set.
2. Leave out the disk, place only the single pixel in the center representing the star. This can be useful for checking if data reduction algorithms work properly.
3. Leave out the star, this way we see what the vAPP does to the extended disk.

For each of the sets we can generate an additional variant to look at what the best result attainable is by leaving out the PSF distortions. We do this by taking the convolution of the n-th disk image with the first PSF of the PSF set instead of the n-th.

We do not try to simulate noise sources as detector or photon noise. These will not affect the disks morphology and the techniques for handling them are the same between disks and other objects.

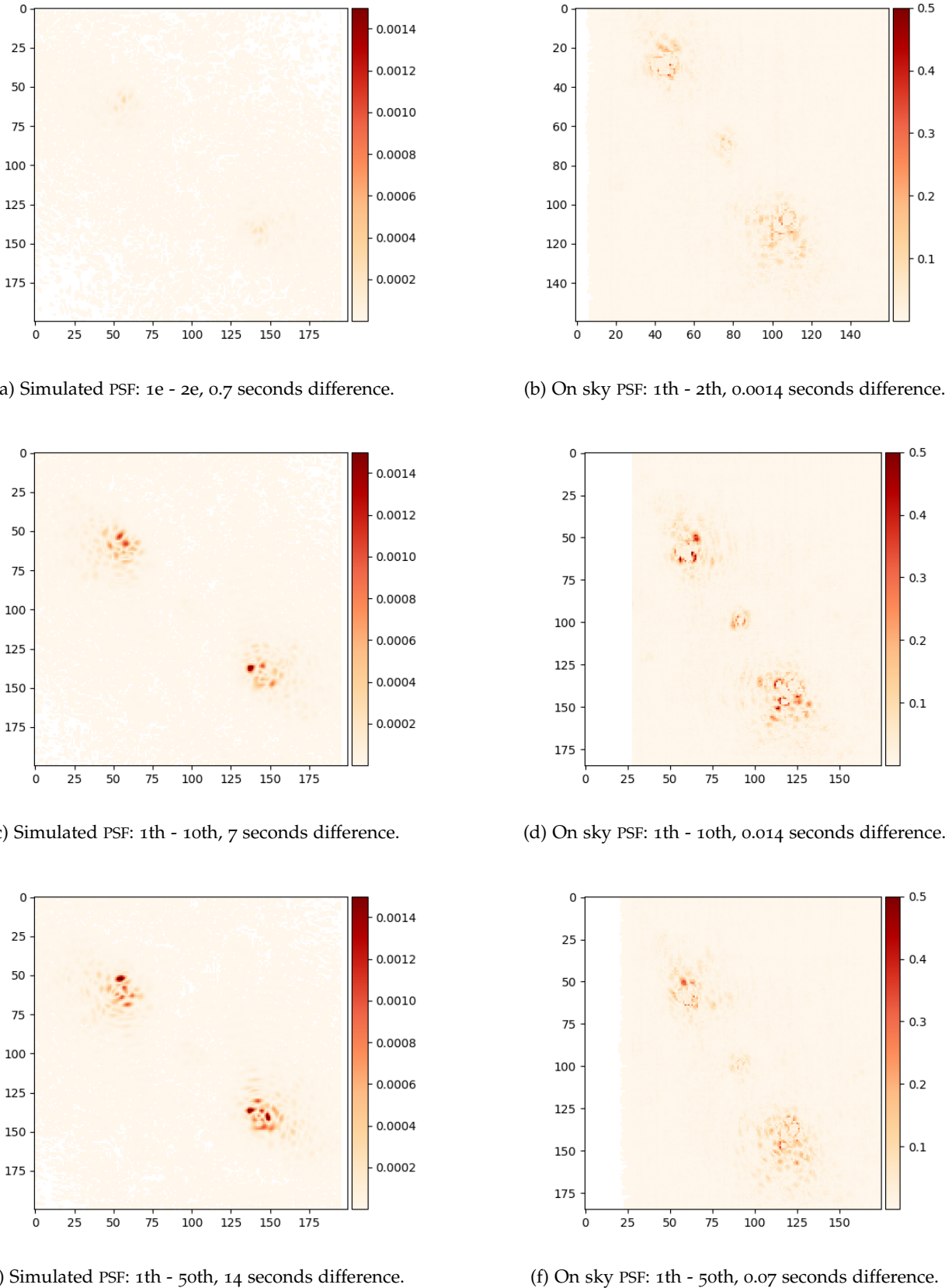


Figure 9: Differences between the first PSF of an observation and later PSFs.

Compared between simulated observations on the left and on-sky data on the right. The PSFs were aligned then normalized on the maximum of the leakage term, finally the absolute value of the difference between the first and n-th PSF was taken. The second, 10th and 50th simulated PSF are 0.7, 7 and 14 seconds apart in simulation time. These give similar morphology to the on sky differences that are 0.0014, 0.014 and 0.07 seconds apart.

4

DATA REDUCTION

The generated images contain 2 mirrored dark zones and are shifted relative to each other by the changing PSFs. Part of ADI is removing the light from a star by subtracting a reference PSF. This does not work if the reference PSF is shifted relative to the PSF of the image. To solve this we create 2 aligned stacks of processed images before applying any post processing technique. Then we use the ADI algorithm to remove star light.

4.1 PRE-PROCESSING

Before we extract the coronagraphic PSFs we align the images. We find the shift relative to the vAPP instrument PSF for every image in the set by cross correlating an up-sampled image. Then the images are shifted using spline interpolation¹. For the implementation of both algorithms we use the SciPy library[6].

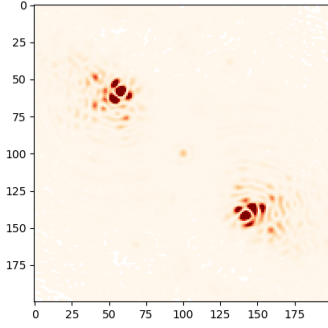
We find the center of the coronagraphic PSFs by splitting the image into a left and right half. For each half the brightest pixel gives the center. Then we create two images by extracting the coronagraphic PSFs. To do this we copy a square with sides of 30% of the original image width around the centers found. These copies are the extracted coronagraphic PSFs. This procedure is repeated for all images this gives 2 aligned stacks, a slice of which can see in [Figure 10b](#) and [Figure 10c](#).

4.2 ANGULAR DIFFERENTIAL IMAGING

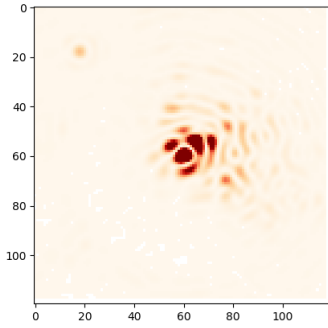
4.2.1 Algorithm

Now there are two separate stacks of images we apply the ADI algorithm [10] to each. First the median is taken over the stack using the implementation provided by the Numpy library [13]. This is our reference PSF. After subtracting the reference PSF from each image we rotated it back so the fields of all images are aligned with respect to the disks major axis (see [Section 3.3](#)). As this means rotating square inside a equally sized square here we lose parts as the right angles of the rotating square rotate out of the equally sized square. The empty space that appears at the right angles is filled with value 0. The pixel values are determined by spline interpolating. For the rotation algorithm we use again the SciPy library [6].

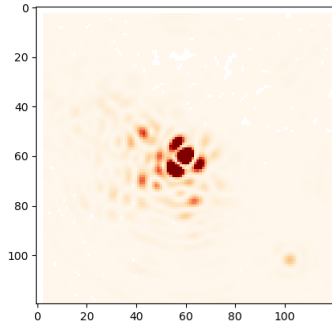
¹ Here an image is interpolated by fitting multiple polynomials called splines



(a) Exposure after alignment.



(b) Left coronagraphic PSF.



(c) Right coronagraphic PSF.

Figure 10: A simulated image after the Pre-processing process, first it was aligned and then its right and left coronagraphic PSF were extracted.

Finally we take the median over the processed images to get a the end result.

4.2.2 Control

We check if the algorithm works applying it to an image set with only the star and no distortions applied. This results in a completely blank image as expected. Next we apply ADI to an image set with only the star and distortions applied. We expect ADI to remove the static part of the vAPP PSF, however the dynamic distortions caused by seeing will rotate during de-rotation. The median of the image will then be a median of the rotated distortions. This will be a circular noise pattern that decreases in intensity towards the edges following the intensity curve of the bright side of the vAPP PSF. The seen circular noise pattern seen in the result (see [Figure 11](#)) confirms our expectation and demonstrates the ADI implementation works.

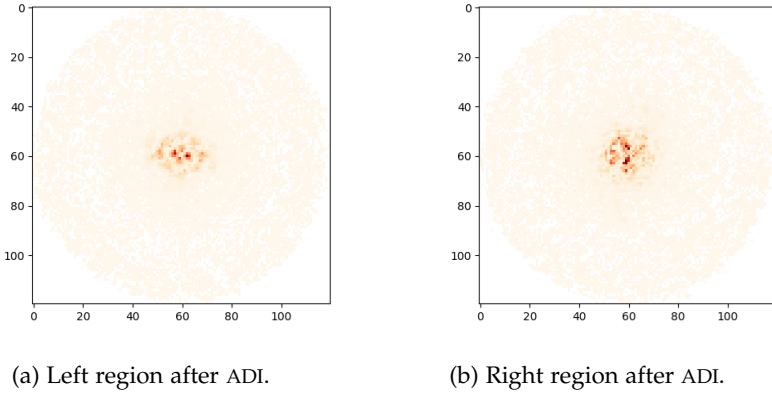


Figure 11: The right and left end result of ADI applied to a generated image stack of a star. The stack contains 20 images, the field rotation over the entire stack is 60° . Note how de-rotating the fields leads to a circular result as we lose the angles.

4.3 PARAMETER STUDY

When observing disks we are most interested in their morphology. It will however be heavily affected by the vAPP and ADI. The uneven redistribution of light by the vAPP will smear the light of the disk changing its apparent morphology. ADI removes rotational symmetry and disks are by nature quite rationally symmetrical thus again the disks apparent morphology will change. To see how the output morphology resembles that of the input model we generate image stacks for a number of disks with different parameters. We vary the number of rings, the width of the rings and the inclination.

For each model we have an additional variant: the *starless* variant has the star in the center of the disk removed. We generate it only using the instrument PSF. It shows what imaging with the vAPP and data reduction using ADI do to the light reflected by the disk. The result of ADI applied to this model indicates what are disk features and what are not on the ADI result of the normal model.

We expect the morphology of the post processed disks to differ from the model's input. However we expect the new morphology to be unique for the input model or some of its parameters.

5

RESULTS

Here we present the results of the parameter study. We have varied the inclination, rotation, number of rings and the sizes of the ring(s). Most disks are variants on the standard disk, its parameters are listed in [Table 1](#). All combinations studied are presented in [Table 2](#).

Throughout this section we show images and ADI results of both various disk models and their *starless* variant see [Section 4.3](#).

Parameter name	value
Time between simulated exposures	0.7 seconds
Fried Parameter	4
Field Rotation	120 degrees
Inclination	60 degrees
Number of images in set	20
Field rotation over set	60 degrees
Number of rings	1
Ring inner radius	30%
Ring outer radius	50%

[Table 1](#): The parameters of the standard disk model. Note the field rotation of 120 degrees is needed to maximize the part of the inclined disk that fits in the dark hole.

First we present a detailed look at a disk with two rings and a disk with only one, see [Figure 12](#) and [Figure 13](#). Then we present the effect of lowering contrast between the star and disk on the generated image and ADI result, see [Figure 14](#). Finally we present 4 comparisons, studying the ADI results for images generated from models with and without star. We compare:

1. A disk with one ring to one with two, see [Figure 15](#).
2. A small and large disk with only one ring, see [Figure 16](#).
3. The standard disk and one disk that has a lower inclination [Figure 17](#)
4. A disk that has been rotated and does not fit the dark hole during the entire rotation, see [Figure 18](#)

Table 2: An overview of all the disks we look at. If a disk has multiple rings their inner and outer dimensions are listed on different lines.

Disk	Figure Numbers	Rings			Inclination (degrees)	Field Rotation (degrees)	Appendix	Note
		Number	Inner and Outer radius (percent of image width)					
A	12 14a 14c 14e	1	30% - 50%		60	120		
	17a 17c 17e							
	18a 18c 18e							
B	13 15a 15c 15e	2	10% - 20%		60	120		
			30% - 40%					
			30% - 50%					
C	14b 14d 14f	1	30% - 50%		60	120	Figure 21 Figure 27	1/6-th normal disk brightness
D	15b 15d 15f	1	30% - 40%		60	120	Figure 22 Figure 28	
	16a 16c 16e	1	10% - 80%		60	120	Figure 23 Figure 29	
E	16b 16d 16f	1	10% - 20%		60	120	Figure 24 Figure 30	
	17b 17d 17f	1	30% - 50%		60	0	Figure 25 Figure 31	
	18b 18d 18f	1	30% - 50%		40	120	Figure 26 Figure 32	

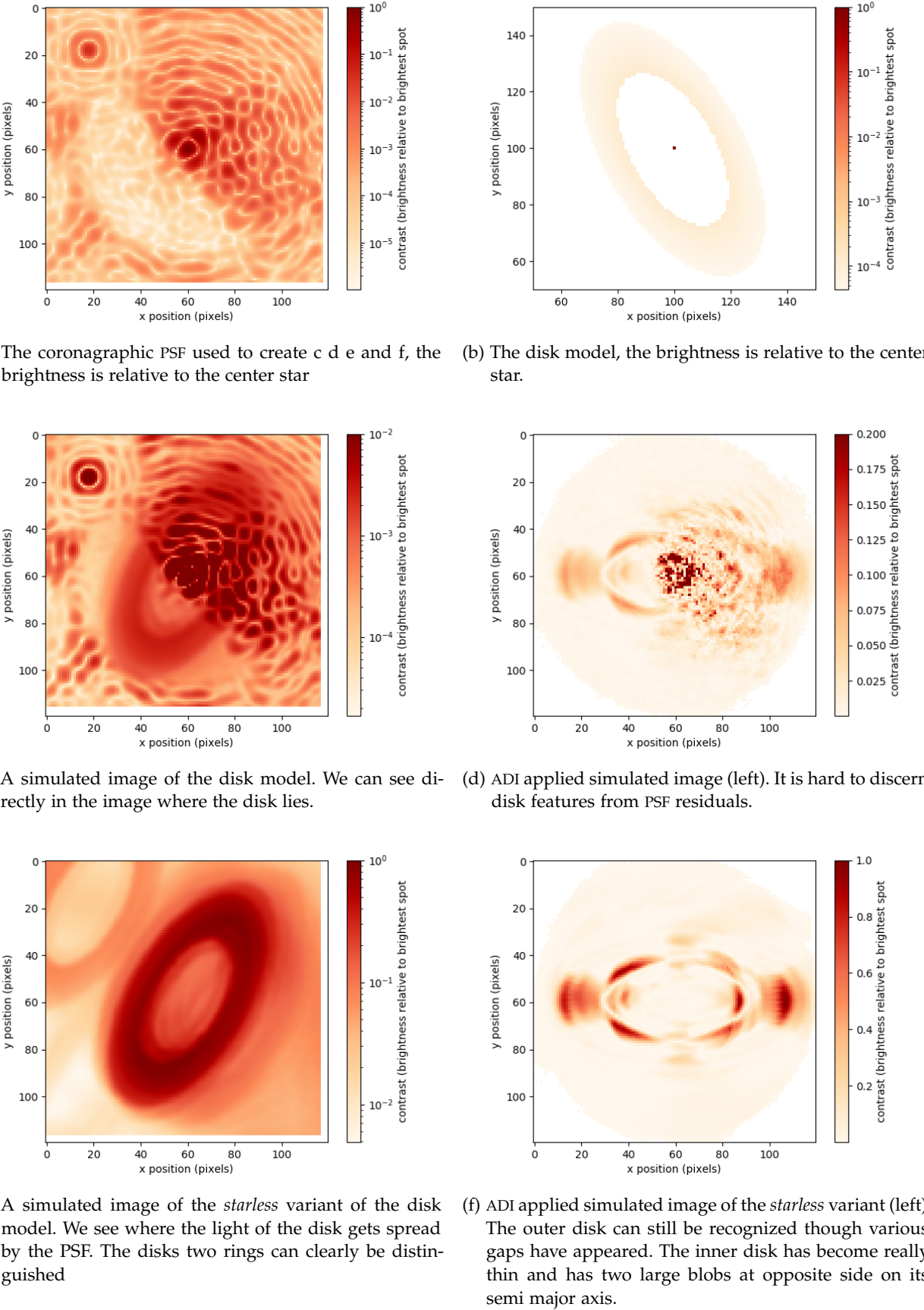


Figure 12: A detailed look at a disk with one rings. On the top row: the PSF and the disk model used to generate the other images. Then generated images of the disk model en its *starless* variant (left) and results of ADI applied to them (right).

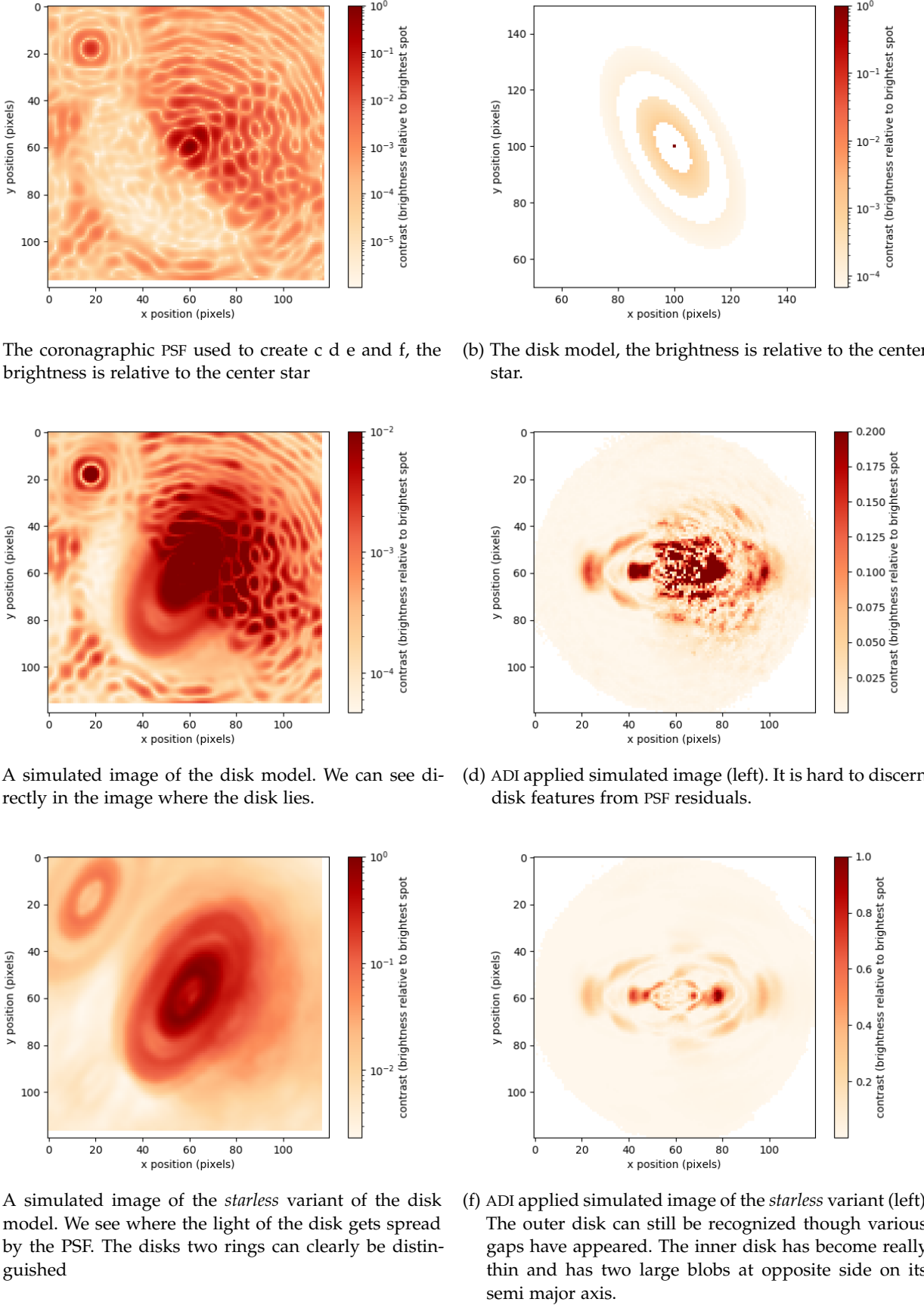


Figure 13: A detailed look at a disk with two rings. On the top row: the PSF and the disk model used to generate the other images. Then generated images of the disk model en its *starless* variant (left) and results of ADI applied to them (right).

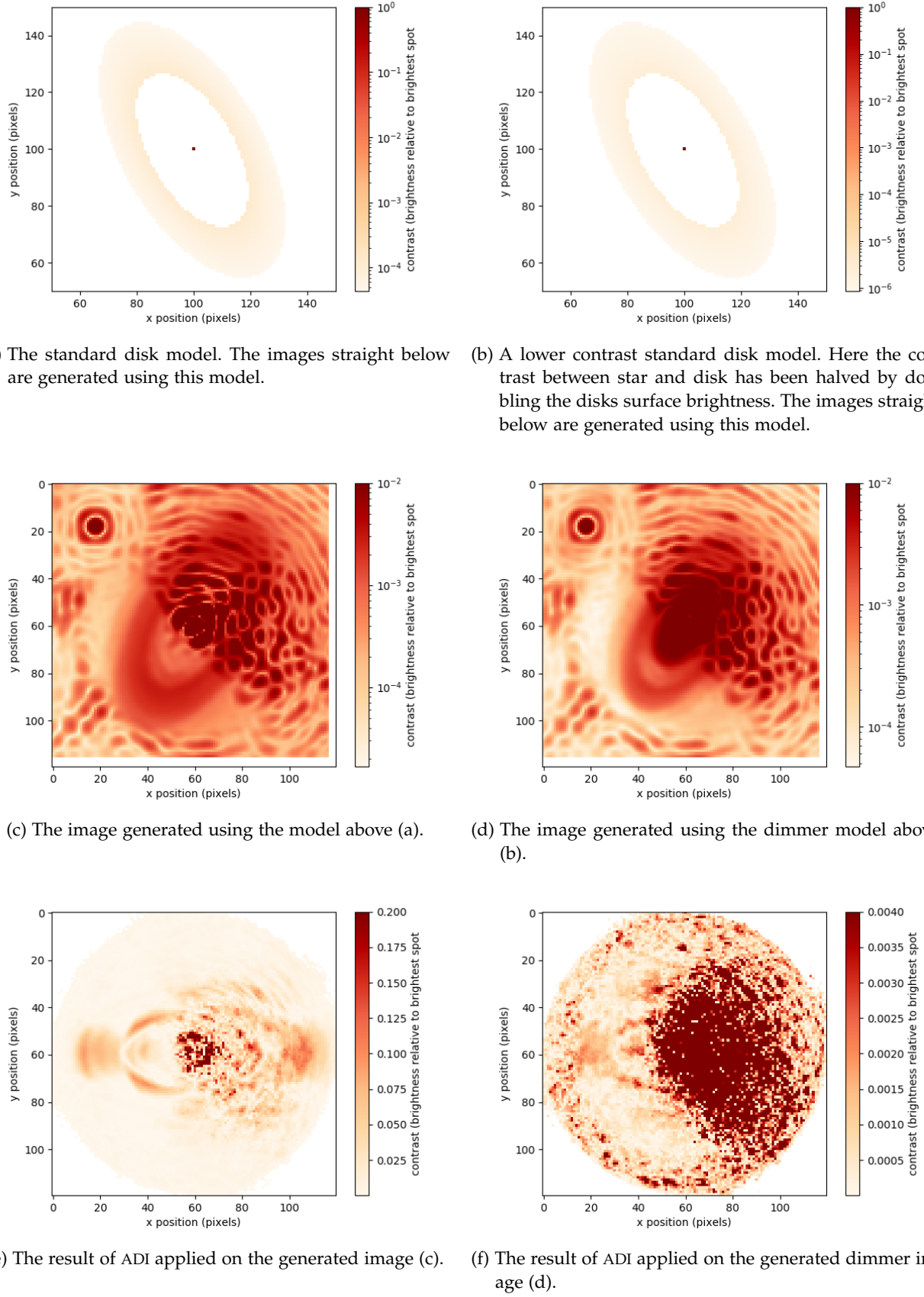


Figure 14: The standard disk model, the image it generates and the result after ADI. The model in the right column has half the contrast between the star and the disk as the left one.

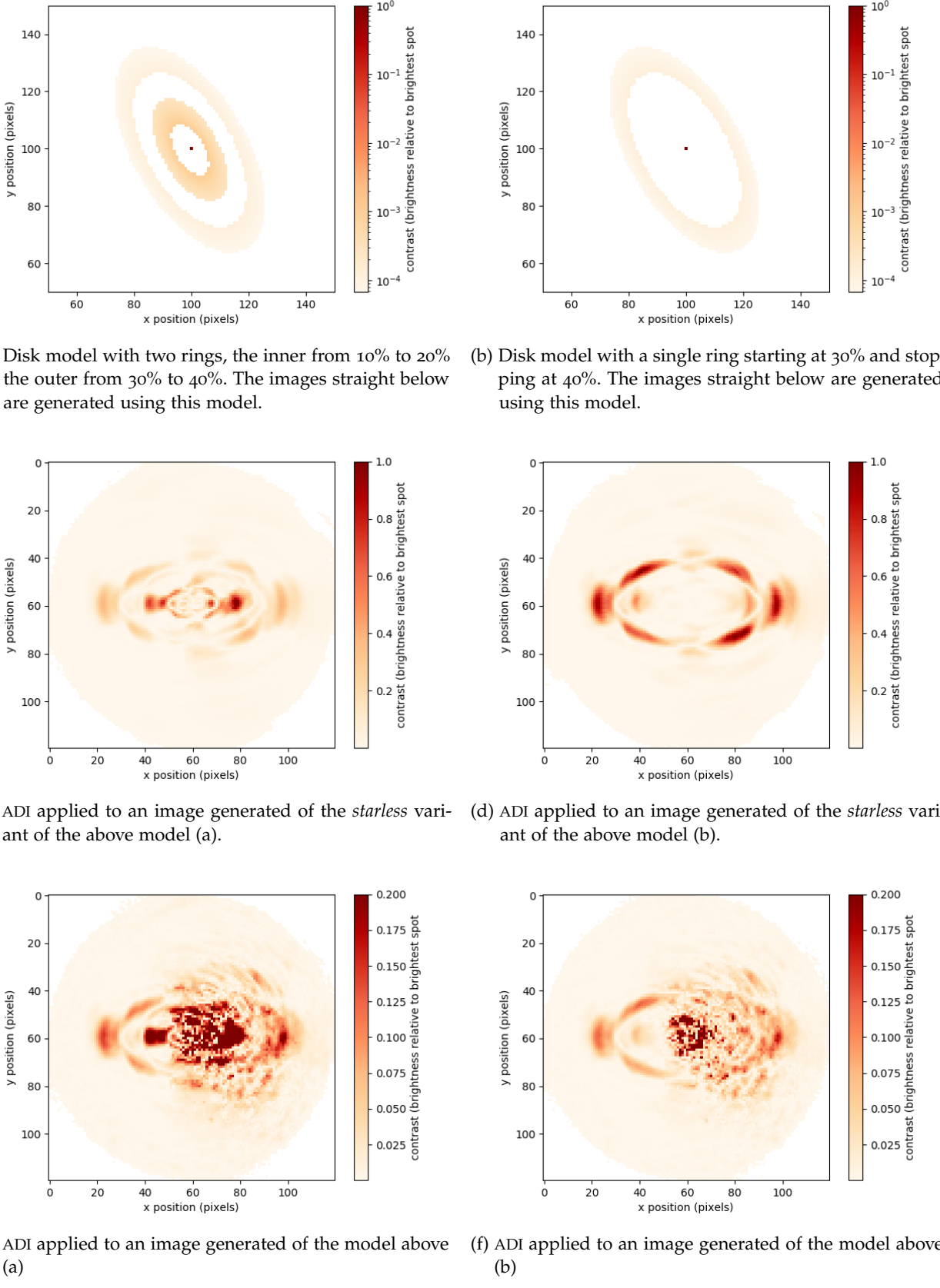


Figure 15: Comparing a disk with two rings with one that has only one ring. Both columns from top to bottom: the disk, ADI applied to a simulated image of only disk and not the star, ADI applied to a simulated image of the disk and star.

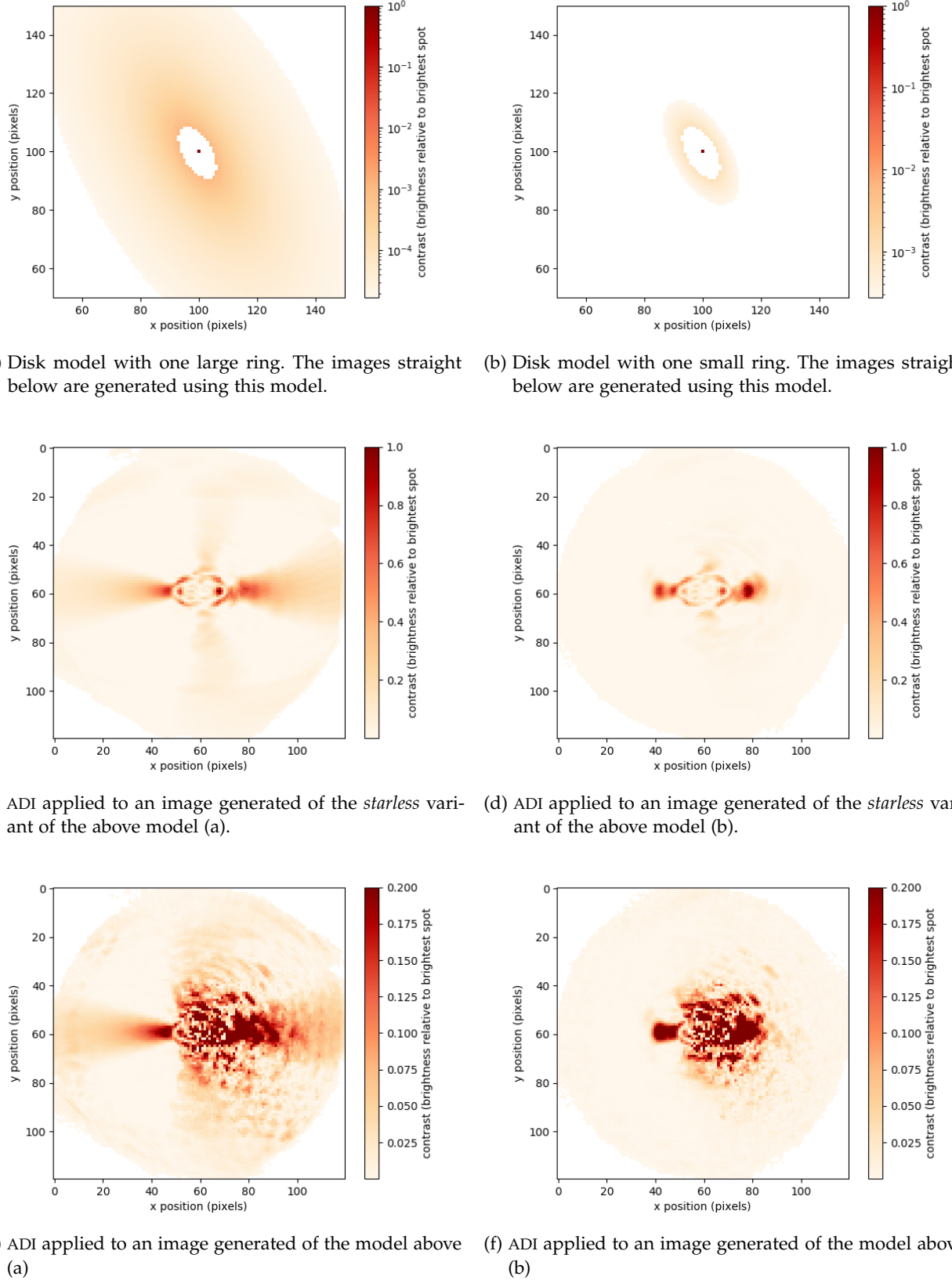


Figure 16: Comparing a large and small disk. Both columns from top to bottom: the disk, ADI applied to a simulated image of only disk and not the star, ADI applied to a simulated image of the disk and star.

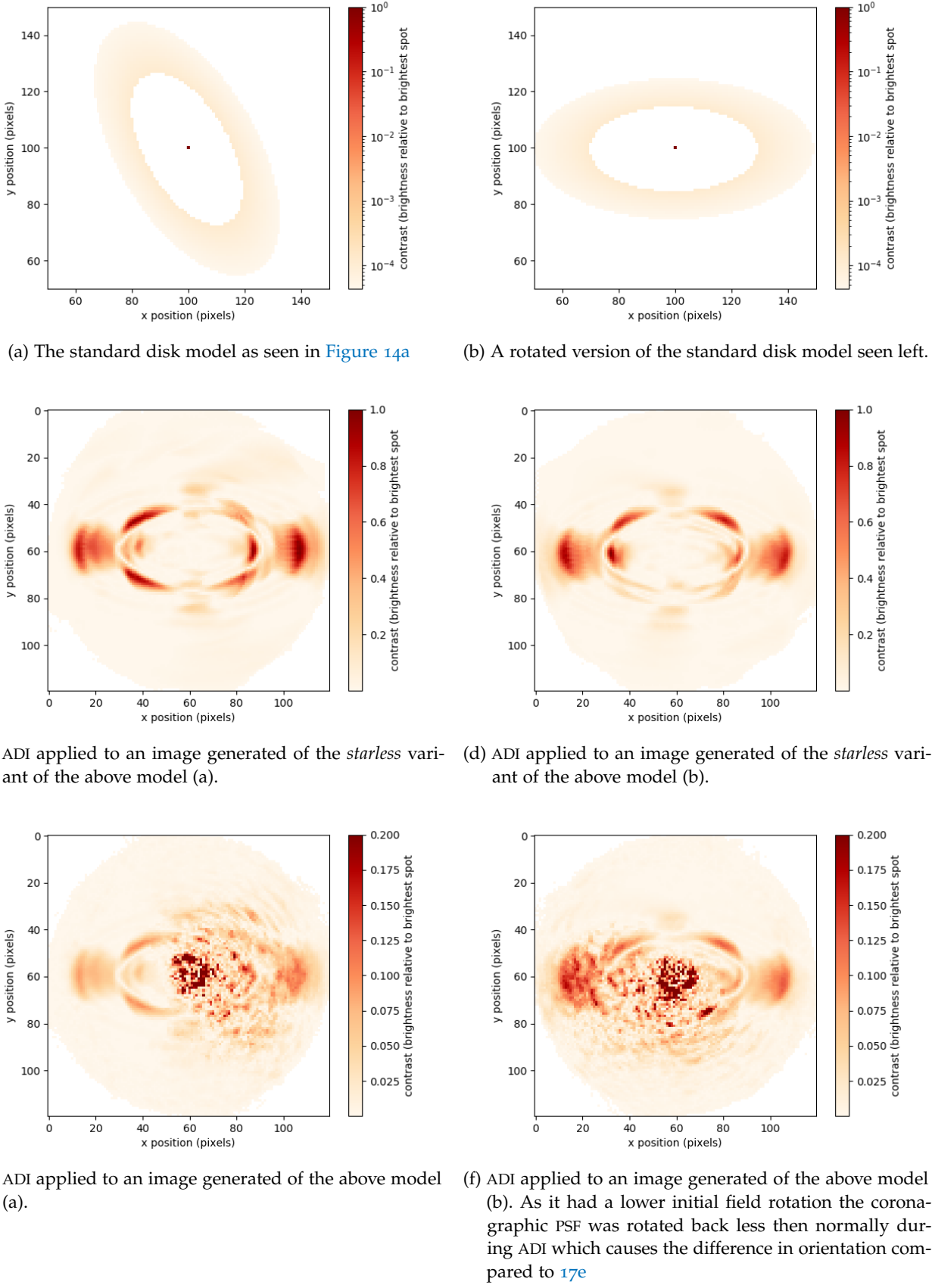


Figure 17: Comparing two disks with different initial field rotation. Both columns from top to bottom: the disk, ADI applied to a simulated image of only disk and not the star, ADI applied to a simulated image of the disk and star.

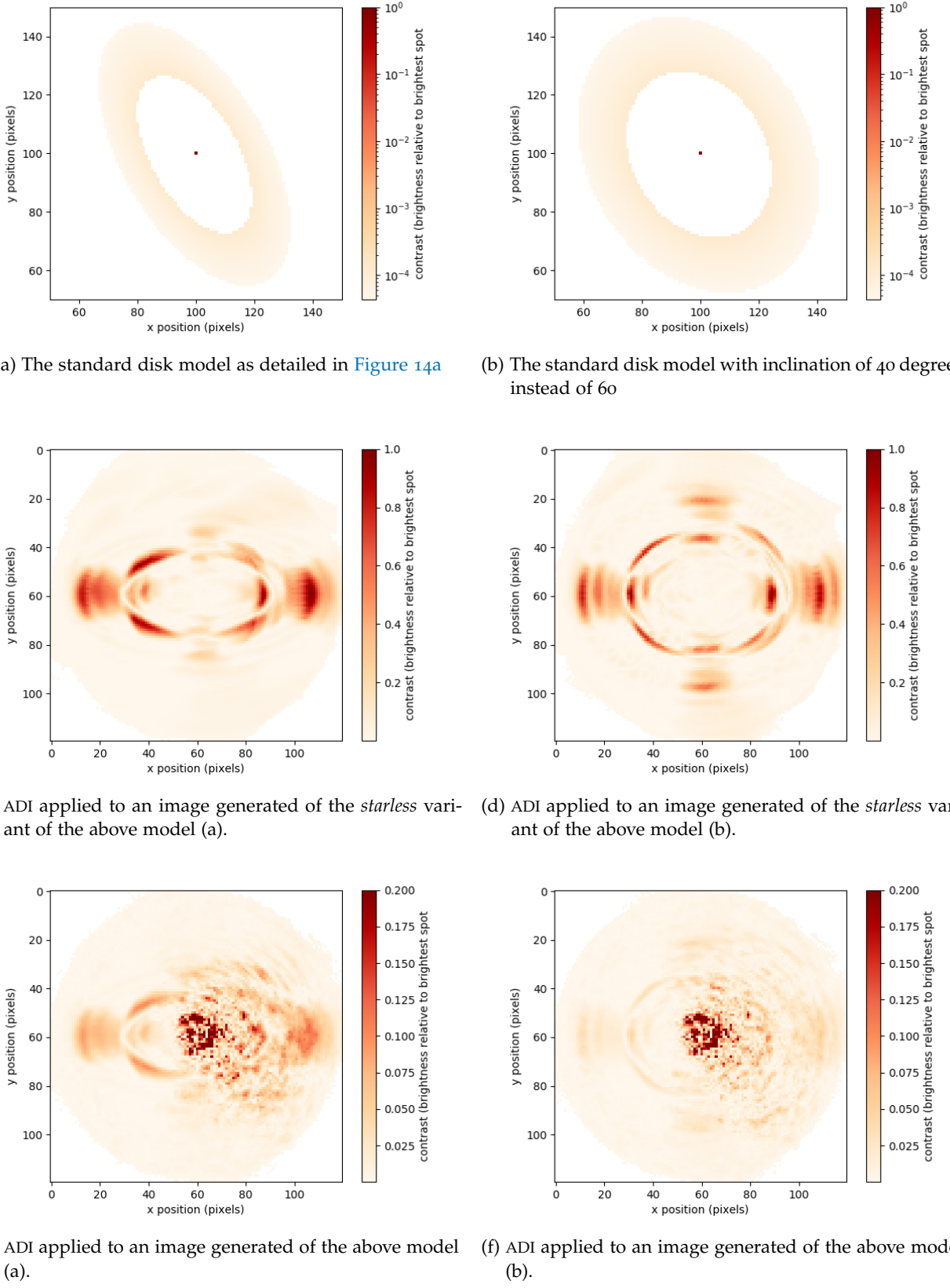


Figure 18: Comparing the standard disk model at 60 and 40 degrees inclination. Both columns from top to bottom: the disk, ADI applied to a simulated image of only disk and not the star, ADI applied to a simulated image of the disk and star.

6

DISCUSSION AND CONCLUSION

Here we discuss the results and conclude whether looking at disks reduced with ADI from vAPP data shows promise. We first take a look at what the vAPP and ADI do to the disk, see the first two figures in [Chapter 5](#). Then we compare different disk models and the result after ADI. We see if we can recognize the original morphology and or we can clearly separate the different models based on the results.

6.1 ADI DISK RESULTS IN DEPTH

Two disks *A* and *B* (see [Table 2](#)) are presented in depth, they are identical except *A* has one rings and *B* two. Looking at the results for disk *A* we can make out the disk in the simulated image in [Figure 12c](#). If we look at [Figure 12e](#) showing only the light reflected by the disk we see that the vAPP has smeared out the light reflected by the disk, the morphology has not been distorted.

When ADI is applied we see ([Figure 12f](#)) that the morphology is radically changed, quite a number of features appear. Most notably bright blobs in the shape of an eighth of a circle appear just outside the disk where the rings semi-major axis intersects the ring. Less bright similarly shaped blobs appear where the rings semi-minor axis intersects the ring.

When ADI is applied to the simulated image (see [Figure 12d](#)) we see residuals from the PSF overlaying the morphologically changed disk in the dark hole. Note that the changed disk is slightly smeared out and faded compared to [Figure 12f](#). This is caused by the atmosphere changing the PSFs and by the ADI process.

Moving on to disk *B*, we find the similar changes as *A*. This disk has a small secondary inner ring. If we look at [Figure 13c](#) we see that only a small part of the inner disk lies in the dark zone. We see in [Figure 13f](#) that the light of the inner ring is concentrated into bright blobs at opposing sides of the rings semi major axis. When we look at the result of ADI on the simulated image of disk *B* (see [Figure 13d](#)) we can recognize the blob. This helps in detection the inner ring.

6.2 ADI FOR DIM DISKS

To see whether ADI applied to vAPP images can help recognize dim disk features, that would otherwise remain hidden in the vAPP dark zones, we compare two identically shaped disks. The first is the standard disk model ([Table 1](#)), the second has its brightness reduced by a

factor 6. While the second disk is still clearly visible in the vAPP dark zone in [Figure 14d](#) it is hardly above the PSF residuals in [Figure 14f](#). ADI does not help us see dim disks.

6.3 CHARACTERIZING PARAMETERS IN ADI RESULTS

The distortions to the disks morphology created by ADI might allow characterization of disks parameters. Here we discuss the results of the four comparisons introduced in [Chapter 5](#) that compare disks with different parameters.

ONE RING VS TWO

We note again the blobs on the semi major axis described in [Section 6.1](#). When we compare the result of ADI applied to the simulated images ([Figure 15e](#) and [15f](#)) we see two blobs for the disk with one rings as well as the disk with two rings. However we can clearly recognize the disk with two rings as its inner blob is brighter than the outer one while the inverse is true for the disk with one ring. We conclude that an inner ring can be recognized by a brighter blob on the semi major axis of a distorted ring.

SMALL VS LARGE DISK

Here two disks are compared each with a ring that starts at the same radius, however the ring of the larger disk stops further out. We first compare the ADI result of the *starless* disk in [Figure 16c](#) and [Figure 16d](#). The features close to the center differ little, these come from the inner part of the ring. Further out we see a large difference. The blobs on the semi-major axis get blurred and have a gradient outwards for the larger disk. We see the same outwards gradient emanating from the semi-minor axis. When we move on to ADI applied to the disk with star ([Figure 16e](#) and [16d](#)) we clearly recognize the outwards gradient coming from the semi-major axis for the large disk. We can also see the blob is blurred more for the large disk.

60 DEGREES INCLINATION VS 90 DEGREES

With a lower inclination we expect worse ADI performance as there is more radial symmetry which leads to increased self subtraction. The shape of the ring after ADI applied to the *starless* disks is more circular for the less inclined disk (see [Figure 18c](#), [Figure 18d](#)). We see the difference between the blobs on the semi-major and semi-minor axis reduce. Further more we notice the intensity of the disk drops as the inclination is reduced. This is caused by self subtraction.

DISK INSIDE DARK HOLE VS OUTSIDE

Here we do not look at a parameter of the disk itself but the way

it was observed. For all other disks an initial field rotation of 120 degrees was used to make sure the disks semi-minor axis was aligned with the straight inside edge of the dark hole. Here we compare a rotated to an un-rotated disk. Looking at ADI applied to the *starless* disk we note the intensity of the lower half of the disk is lower for the un-rotated disk ([Figure 17d](#)) compared to the rotated disk ([Figure 17c](#)). Taking a look at the result of ADI applied to the disk with star we see a larger portion of the disk result lies amid the residuals of the PSF obscuring more of the disk.

6.4 CONCLUSION

Observing disks with the vAPP has similar advantages to observing exoplanets with the vAPP. Disk features can be recognized clearly up until they are very close to the center of the coronagraphic PSF peak. The vAPP does significantly smear out the image of the ring which makes it harder to look at lower contrast disk features such as gradients or soft edges. A fitting routine factoring in the smearing effect of the vAPP might be able to combat this.

Applying ADI to the simulated images reveals disks are heavily distorted due to self subtraction. This problem is not be unique to observing disks with an asymmetrical PSF such as the one of the vAPP. Classical instruments with a symmetrical PSF will suffer the same problem. As the inclined disk rotates, its extremes, where the disk crosses the semi minor and semi major axis, suffer the least self subtraction.

We see an example of this effect in its extreme in [Figure 19](#). Here we see the result of ADI over 360 degrees (a), to illustrate the most extreme case of self subtraction. In [Figure 19b](#) we see the mentioned cause of the self subtraction, note how the outer part of the disk that cross the semi major axis lie outside the blue circle. Inside the circle the parts of multiple disks overlap. The area outside the blue ring well not be impacted by self subtraction. When we increase the number of images or decrees the field rotation the blue ring moves outwards and more self subtraction happens.

The morphology of the distortions does not change when we radically adjust the inclination from 60 to 40 degrees. ADI concentrates the disks light on the semi-major axis of the disks from which an outward gradient of light starts. In a similar way, though at far lower brightness, some light is concentrated on the semi minor axis. The ratio of brightness of these concentrated points between the semi-major and minor axis relates to the inclination of the disk. The extend and intensity of the outward gradient relates to the size of the ring from which it starts. Multiple rings are represented by multiple concentrations of light.

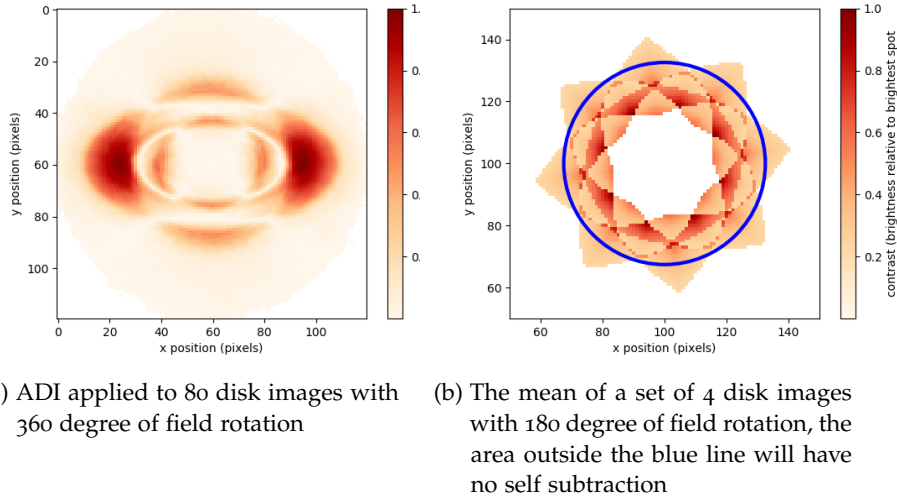


Figure 19: Comparing the extreme of ADI self subtraction at a unrealistic 360 degrees of field rotation to the cause of the self subtraction, the median of the set of images. Both use the vAPP PSF

As ADI deforms the disk heavily we need to recognize distortions to have an idea what the actual disk might look like. In most cases this makes ADI not that useful for observe disks. It might be useful at few λ/D . Since it concentrates light on the semi major axis and has an outward radius small inner rings can be recognized closer to the PSF peak then in the unprocessed image. Improvements to the used ADI method might further refine these results. Though we recommend further studies look into post processing methods that are less prone to self subtraction. We make a few suggestions in the next section.

7

FUTURE WORK

There are a number of ways to improve the results. We advise to look into Reference star Differential Imaging (RDI) instead of ADI. RDI will have far less self subtraction than ADI and good results have been achieved imaging disks with RDI and coronagraph [19] without self-subtraction artifacts.

For RDI an observer collects reference images from stars observed on the same night or from an archive. Then an PSF reconstruction algorithm is used on those reference images [19]. Finally the reference is subtracted from the target image. This will subtract the speckle pattern while limiting self-subtraction [7]. A major challenge with RDI is creating a good reference PSF.

The ADI routine might be improved using only a few images as close in time as possible as reference sequence [10]. As the instrument PSF has evolved less the complete PSFs are more similar and ADI will remove more speckles. If done improperly however this can increase self subtraction. The main source for the artifacts is self subtraction of the disk. When the mean image of the input is subtracted from all the input images pixel values might become negative. These should never be negative exposure. Clipping the *input with mean subtracted* to a minimum value of zero might reduce self subtraction artifacts.

As the disks are heavily deformed after ADI trying to fit the result ADI result to *starless* disk models with ADI applied could help find the parameters of the disk. This could even be extended to training a neural network to generate a disk model given an output of ADI.

Finally fitting a general disk model to the observed image would work well in detecting disks however it will be challenging to find undiscovered or detailed features.

BIBLIOGRAPHY

- [1] A. P. Boss. "Giant planet formation by gravitational instability." In: *Science* 276 (1997), pp. 1836–1839. doi: [10.1126/science.276.5320.1836](https://doi.org/10.1126/science.276.5320.1836).
- [2] David S. Doelman, Frans Snik, Nathaniel Z. Warriner, and Michael J. Escuti. "Patterned liquid-crystal optics for broadband coronagraphy and wavefront sensing." In: *Proceedings SPIE 10400, Techniques and Instrumentation for Detection of Exoplanets VIII* (2017).
- [3] Antonio Garufi et al. "Evolution of protoplanetary disks from their taxonomy in scattered light: spirals, rings, cavities, and shadows." In: (Oct. 2018).
- [4] Okko van der Haak and Pieter Speelman. "Stellar disk reconstruction using Spectro-polarimetry." Bachelor Thesis. June 2018.
- [5] Eugene Hecht. *Optics. International Edition*. Pearson, 2002.
- [6] Eric Jones, Travis Oliphant, Pearu Peterson, et al. *SciPy: Open source scientific tools for Python*. [Online; accessed 21 may 2019]. 2001–. URL: <http://www.scipy.org/>.
- [7] R. Ligi et al. "Investigation of the inner structures around HD 169142 with VLT/SPHERE." In: *Monthly Notices of the Royal Astronomical Society* 473.2 (2018), pp. 1774–1783. doi: [10.1093/mnras/stx2318](https://doi.org/10.1093/mnras/stx2318). arXiv: [1709.01734 \[astro-ph.EP\]](https://arxiv.org/abs/1709.01734).
- [8] Giuseppe Lodato et al. "The newborn planet population emerging from ring-like structures in discs." In: *Monthly Notices of the Royal Astronomical Society* 486 (Mar. 2019), pp. 453–461.
- [9] Christian Marois, R. Doyon, R. Racine, D. Nadeau, D. Lafreniere, P. Vallee, M. Riopel, and B. Macintosh. "Direct Exoplanet Imaging around Sun-like Stars: Beating the Speckle Noise with Innovative Imaging Techniques." In: *Journal of the Royal Astronomical Society of Canada* 99.4 (2005), p. 130.
- [10] Christian Marois, David Lafreniere, Rene Doyon, Bruce Macintosh, and Daniel Nadeau. "Angular Differential Imaging: A Powerful High-Contrast Imaging Technique." In: *The Astrophysical Journal* 641.1 (2006), pp. 556–564. doi: [10.1086/500401](https://doi.org/10.1086/500401). URL: <https://doi.org/10.1086%2F500401>.
- [11] Ian S. McLean. *Electronic Imaging in Astronomy*. Springer, 2008.
- [12] Matías Montesinos, Sebastian Perez, Simon Casassus, Sebastian Marino, Jorge Cuadra, and Valentin Christiaens. "Spiral Waves Triggered by Shadows in Transition Disks." In: *The Astrophysical Journal Letters* 823.1, L8 (2016), p. L8. doi: [10.3847/2041-8205/823/1/L8](https://doi.org/10.3847/2041-8205/823/1/L8). arXiv: [1601.07912 \[astro-ph.EP\]](https://arxiv.org/abs/1601.07912).

- [13] Travis Oliphant. *NumPy: A guide to NumPy*. USA: Trelgol Publishing. [Online; accessed 22 may 2019]. 2006-. URL: <http://www.numpy.org/>.
- [14] Gilles P. P. L. Otten et al. “On-sky Performance Analysis of the Vector Apodizing Phase Plate Coronagraph on MagAO/Clio2.” In: *The Astrophysical Journal* 834.2, 175 (2017), p. 175. doi: [10.3847/1538-4357/834/2/175](https://doi.org/10.3847/1538-4357/834/2/175). arXiv: [1702.04193 \[astro-ph.IM\]](https://arxiv.org/abs/1702.04193).
- [15] C. Perrot et al. “Discovery of concentric broken rings at sub-arcsec separations in the HD 141569A gas-rich, debris disk with VLT/SPHERE.” In: *Astronomy & Astrophysics* 590, L7 (2016), p. L7. doi: [10.1051/0004-6361/201628396](https://doi.org/10.1051/0004-6361/201628396). arXiv: [1605.00468 \[astro-ph.EP\]](https://arxiv.org/abs/1605.00468).
- [16] James B. Pollack, Olenka Hubickyj, Peter Bodenheimer, Jack J. Lissauer, Morris Podolak, and Yuval Greenzweig. “Formation of the Giant Planets by Concurrent Accretion of Solids and Gas.” In: *Icarus* 124.1 (1996), pp. 62–85. doi: [10.1006/icar.1996.0190](https://doi.org/10.1006/icar.1996.0190).
- [17] E. H. Por, S. Y. Haffert, V. M. Radhakrishnan, D. S. Doelman, M. Van Kooten, and S. P. Bos. “High Contrast Imaging for Python (HCIPy): an open-source adaptive optics and coronagraph simulator.” In: *Adaptive Optics Systems VI*. Vol. 10703. Proc. SPIE. 2018. doi: [10.1117/12.2314407](https://doi.org/10.1117/12.2314407). URL: <https://doi.org/10.1117/12.2314407>.
- [18] M. Reggiani et al. “VizieR Online Data Catalog: Angular differential imaging of MCW 758 (Reggiani+, 2018).” In: *VizieR Online Data Catalog*, J/A+A/611/A74 (2017), J/A+A/611/A74.
- [19] Gareth Ruane et al. “Reference Star Differential Imaging of Close-in Companions and Circumstellar Disks with the NIRC2 Vortex Coronagraph at the W. M. Keck Observatory.” In: *The Astrophysical Journal* 157.3, 118 (2019), p. 118. doi: [10.3847/1538-3881/aafcc](https://doi.org/10.3847/1538-3881/aafcc). arXiv: [1901.04090 \[astro-ph.IM\]](https://arxiv.org/abs/1901.04090).
- [20] Frans Snik, Gilles Otten, Matthew Kenworthy, Matthew Miskiewicz, Michael Escuti, Christopher Packham, and Johanan Codona. “The Vector-APP: a Broadband Apodizing Phase Plate that yields Complementary PSFs.” In: *Proc SPIE* 8450 (July 2012). doi: [10.1117/12.926222](https://doi.org/10.1117/12.926222).
- [21] Jonathan Williams and Lucas Cieza. “Protoplanetary Disks and Their Evolution.” In: *Annual Review of Astronomy and Astrophysics - ANNU REV ASTRON ASTROPHYS* 49 (Mar. 2011). doi: [10.1146/annurev-astro-081710-102548](https://doi.org/10.1146/annurev-astro-081710-102548).
- [22] Harold W. Yorke, Peter Bodenheimer, and Gregory Laughlin. “The Formation of Protostellar Disks. I. 1 M sub sun.” In: *The Astrophysical Journal* 411 (1993), p. 274. doi: [10.1086/172827](https://doi.org/10.1086/172827).

APPENDIX

7.1 FOURIER METHOD

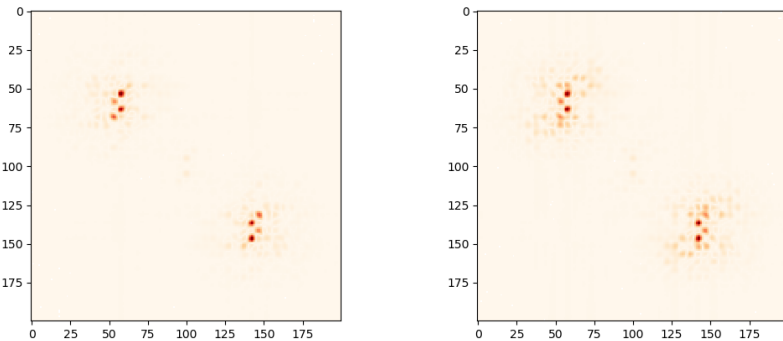
Before we used HCIPy we tried modifying a single given vAPP PSF to get a set of disturbed PSFs. To achieve this a pattern is added to the Fourier transform of the PSF before transforming it back from Fourier space, see [Equation 6](#) below. The pattern is then shifted for every timestamp.

$$I_{\text{final}} = \mathcal{F}_{2d}^{-1} \left(\text{intensity} \cdot \mathcal{F}_{2d}(\text{PSF}) \cdot \text{pattern} + (1 - \text{intensity}) \cdot \mathcal{F}_{2d}(\text{PSF}) \right) \quad (6)$$

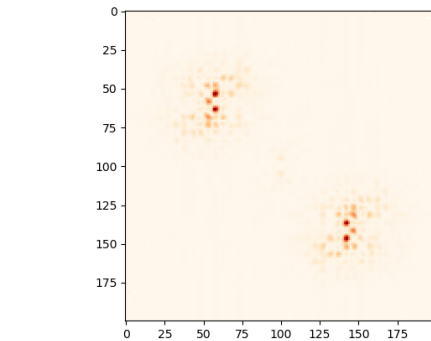
Here "intensity" is a number between 0 and 1, \mathcal{F}_{2d}^{-1} the inverted 2d Fourier transform and \mathcal{F}_{2d} the normal 2d Fourier transform.

The best results where achieved using a grid of blurred circles as pattern, see [Figure 20](#). Note the distortions to the PSF are around the center of its peaks but not randomly spread. As clearly this clearly does not suffice to simulate realistic distortions.

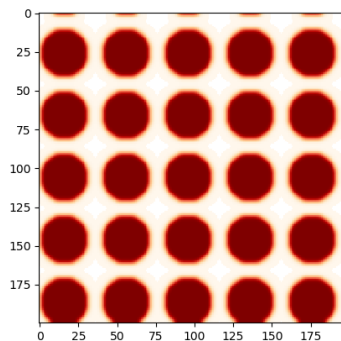
Eventually we chose not to pursue this way further as its only advantage to is that one does not need a description of the instrument and only a single PSF while it performs way worse then a naive simulation.



(a) Difference between two PSFs created using this method, between PSFs the pattern has shifted 10 pixels.



(b) Difference between two PSFs created using this method, between PSFs the pattern has shifted 5 pixels.



(c) Pattern that is shifted and applied to the Fourier space of a PSF.

Figure 20: The Pattern used and the differences between PSFs distorted with it using the method described above.

7.2 LEFT CORONOGRAPHIC PSFS

Figures of the left coronographic PSFs for all disks seen in [Chapter 5](#).
For the right side see the next chapter of this appendix.

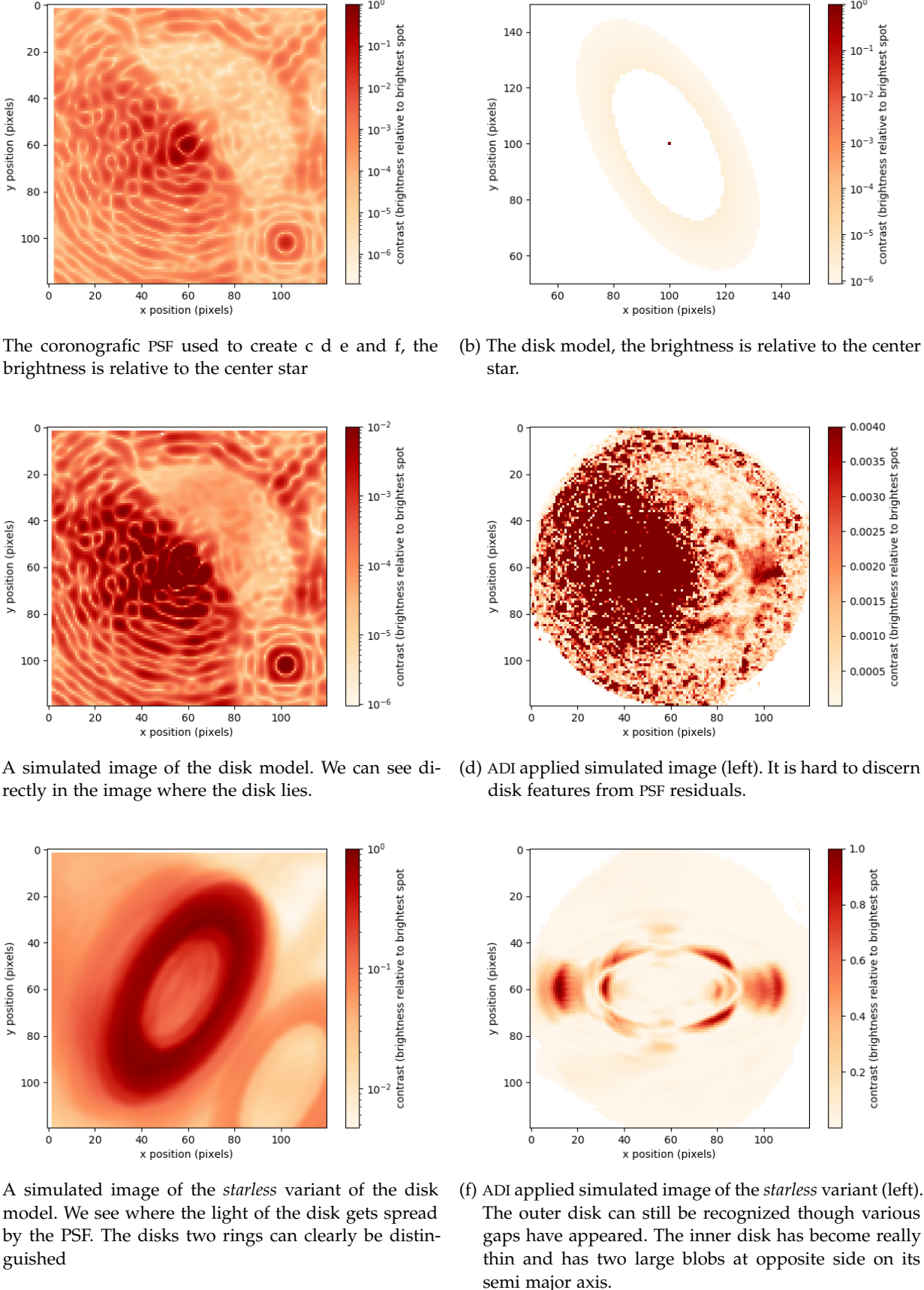


Figure 21: On the top row: the PSF and the disk model used to generate the other images. Then generated images of the disk model en its *starless* variant (left) and results of ADI applied to them (right).

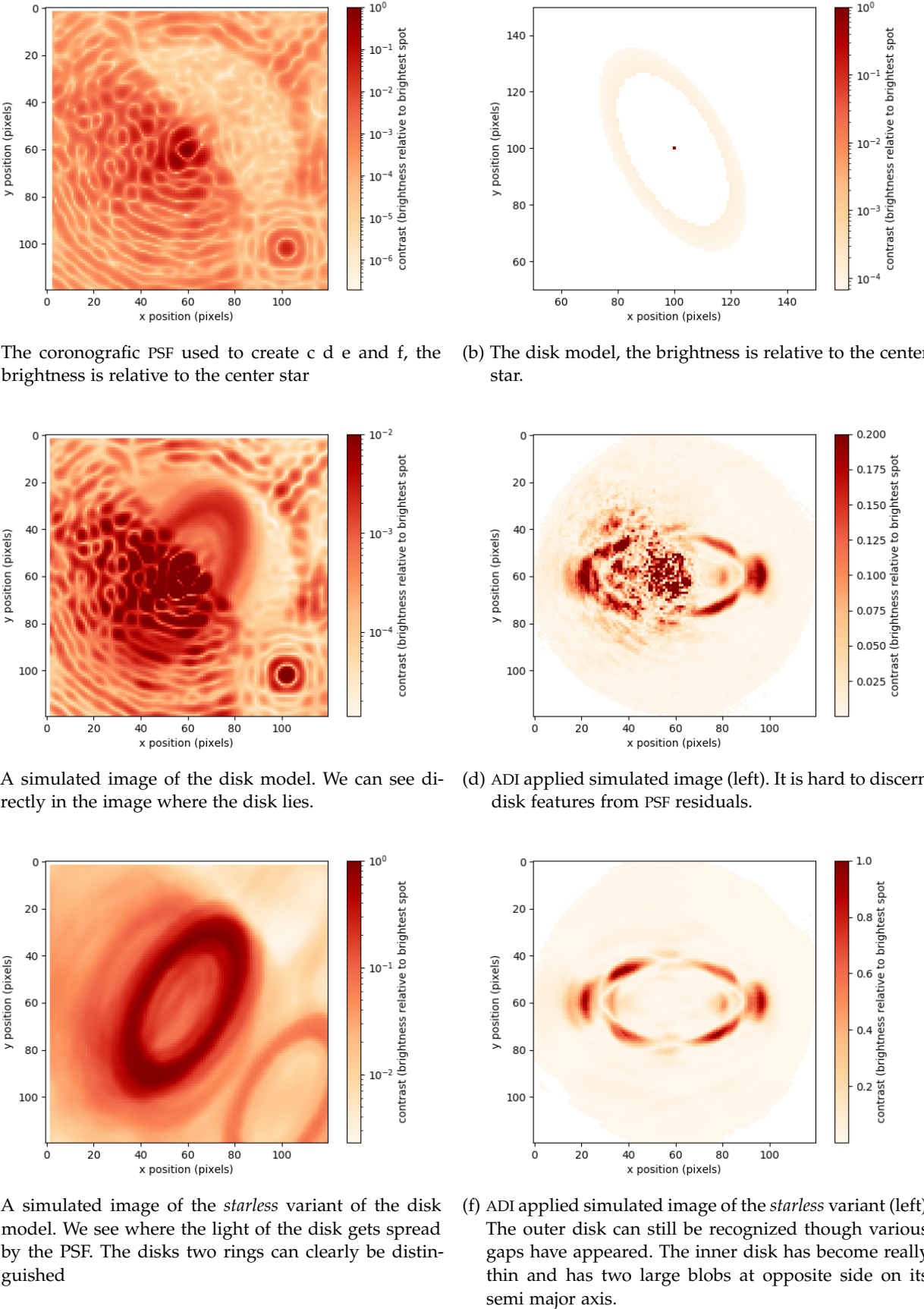


Figure 22: On the top row: the PSF and the disk model used to generate the other images. Then generated images of the disk model en its *starless* variant (left) and results of ADI applied to them (right).

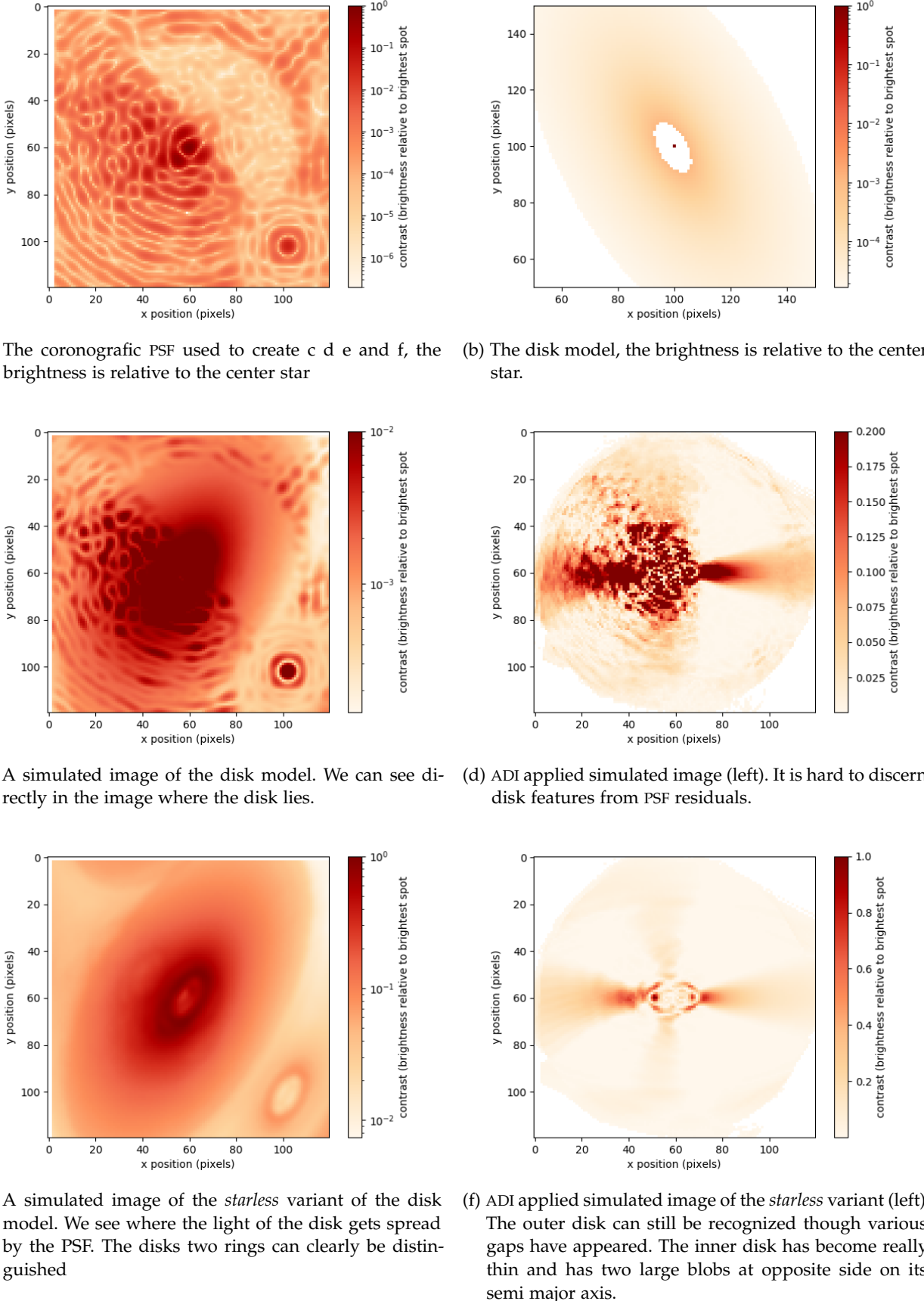


Figure 23: On the top row: the PSF and the disk model used to generate the other images. Then generated images of the disk model en its *starless* variant (left) and results of ADI applied to them (right).

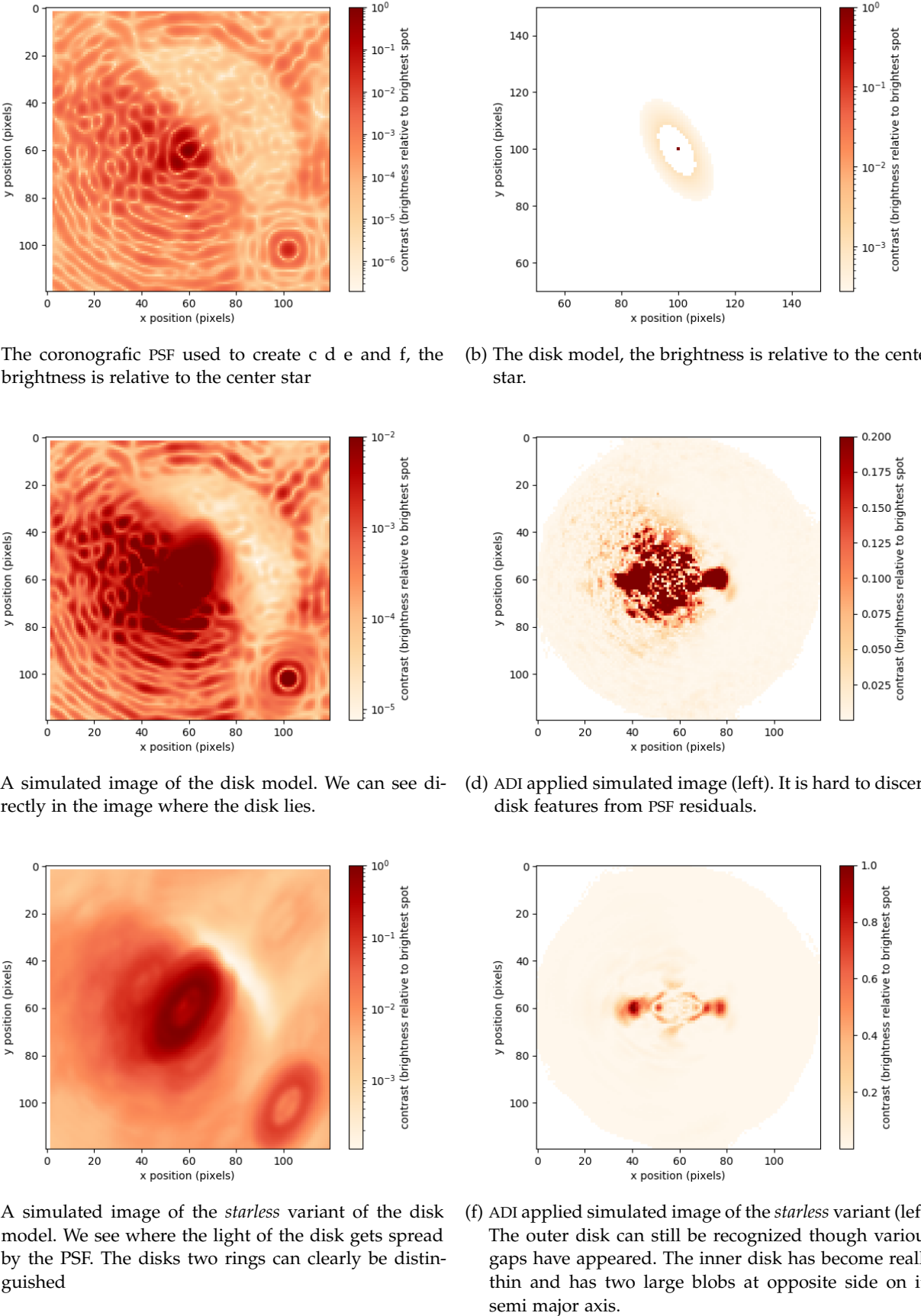


Figure 24: On the top row: the PSF and the disk model used to generate the other images. Then generated images of the disk model en its *starless* variant (left) and results of ADI applied to them (right).

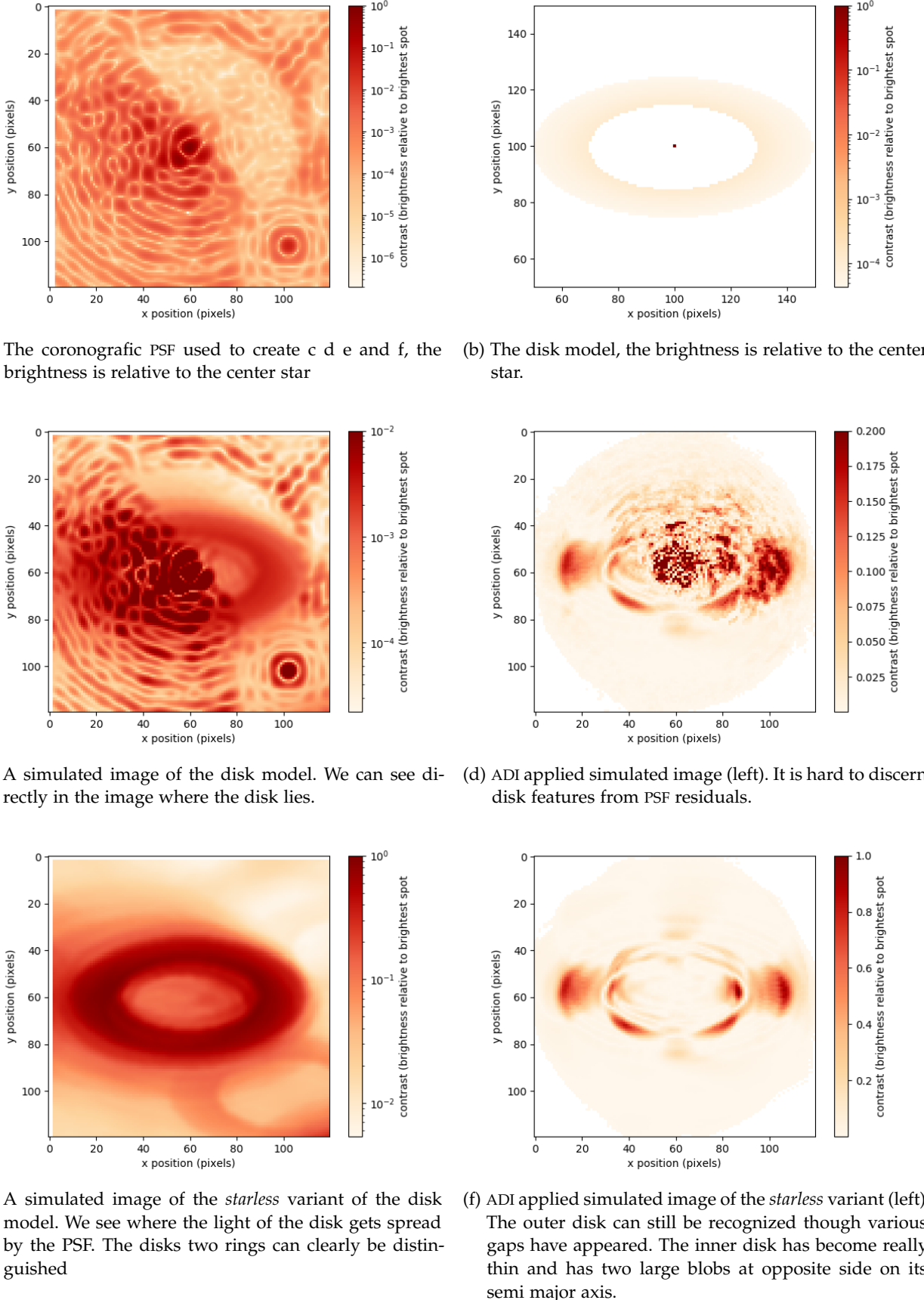


Figure 25: On the top row: the PSF and the disk model used to generate the other images. Then generated images of the disk model en its *starless* variant (left) and results of ADI applied to them (right).

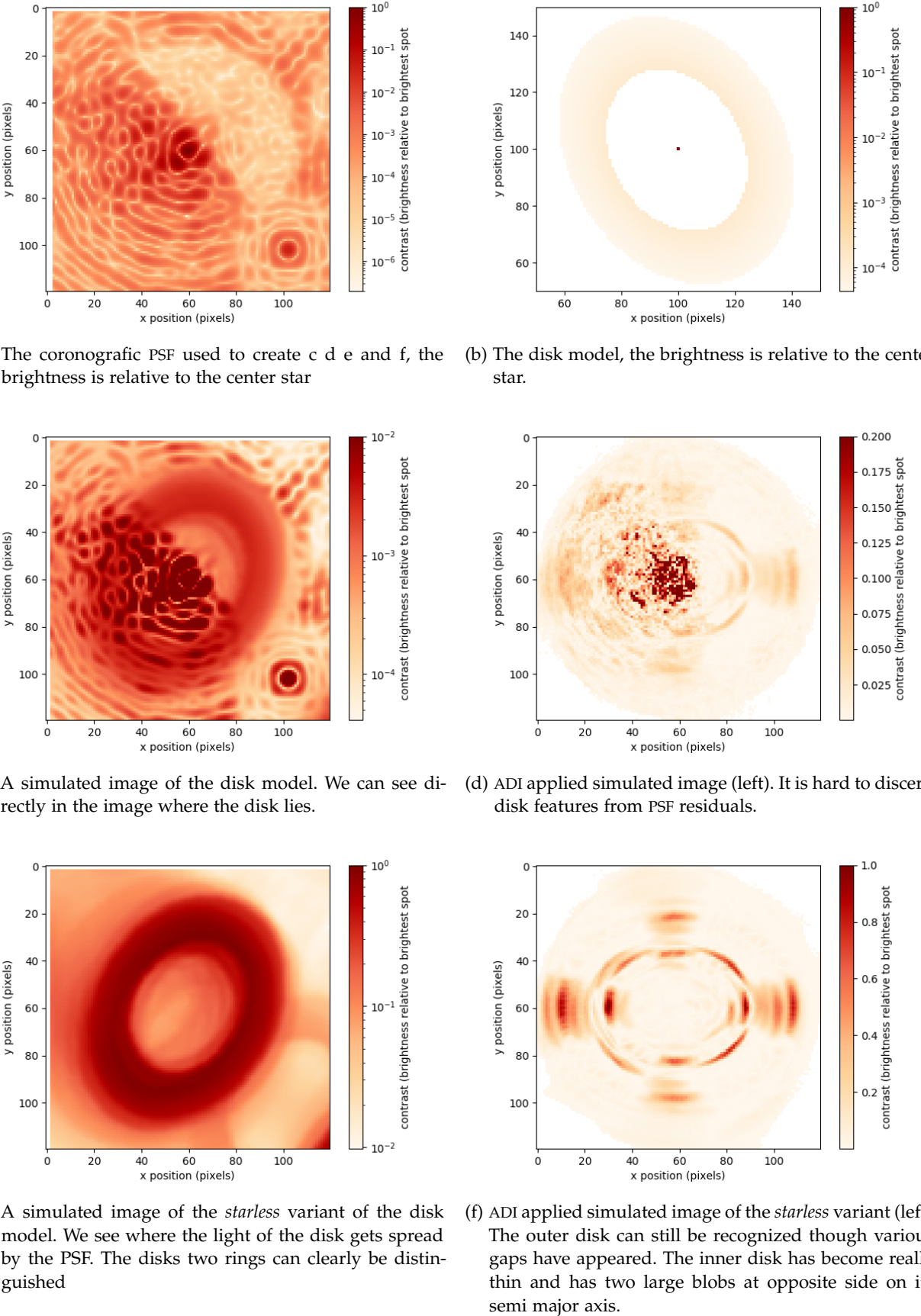


Figure 26: On the top row: the PSF and the disk model used to generate the other images. Then generated images of the disk model en its *starless* variant (left) and results of ADI applied to them (right).

7.3 RIGHT CORONOGRAPHIC PSFS

Figures of the right coronographic PSFs for all disks seen in [Chapter 5](#).
For the left side see the previous chapter of this appendix.

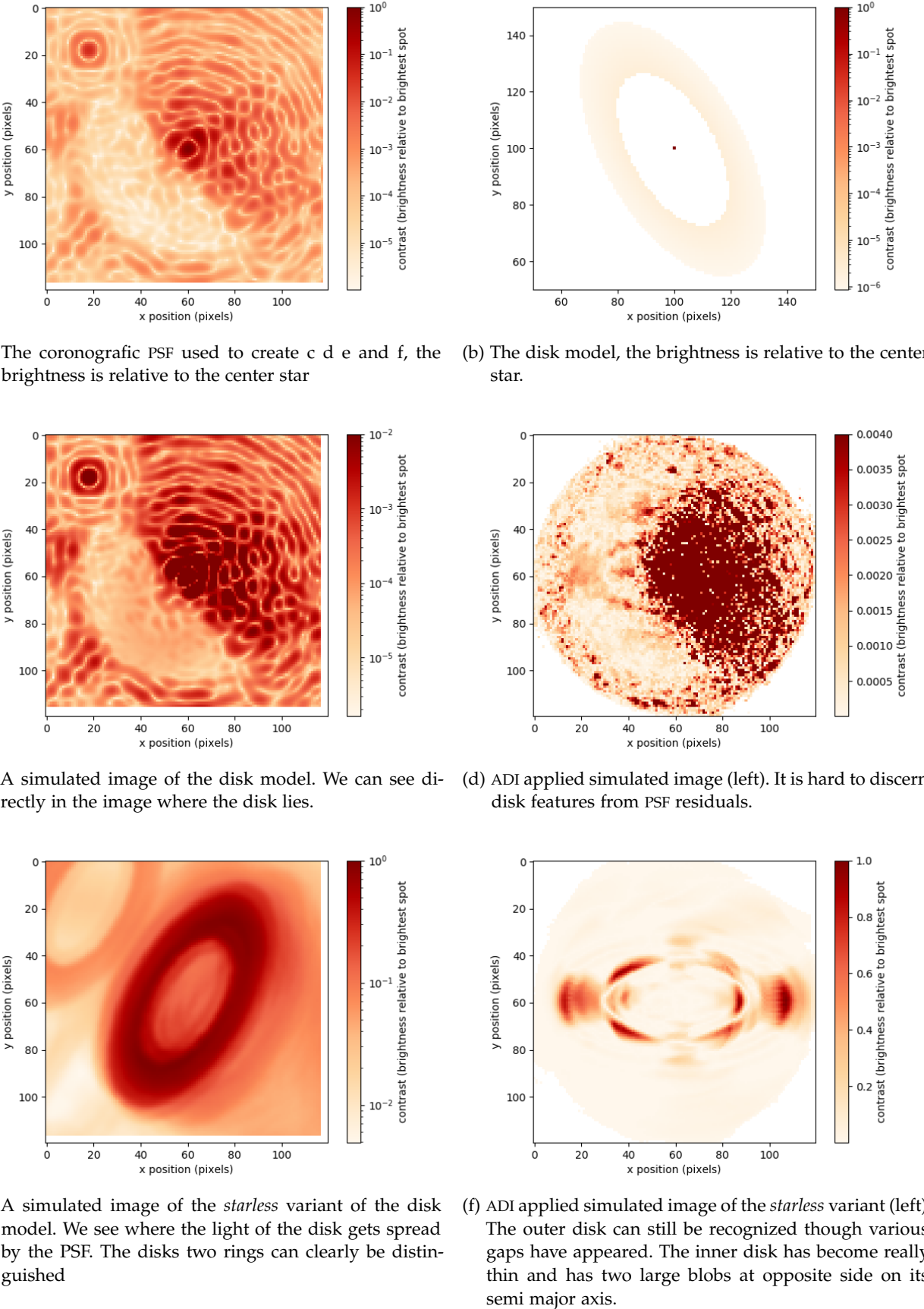


Figure 27: On the top row: the PSF and the disk model used to generate the other images. Then generated images of the disk model en its *starless* variant (left) and results of ADI applied to them (right).

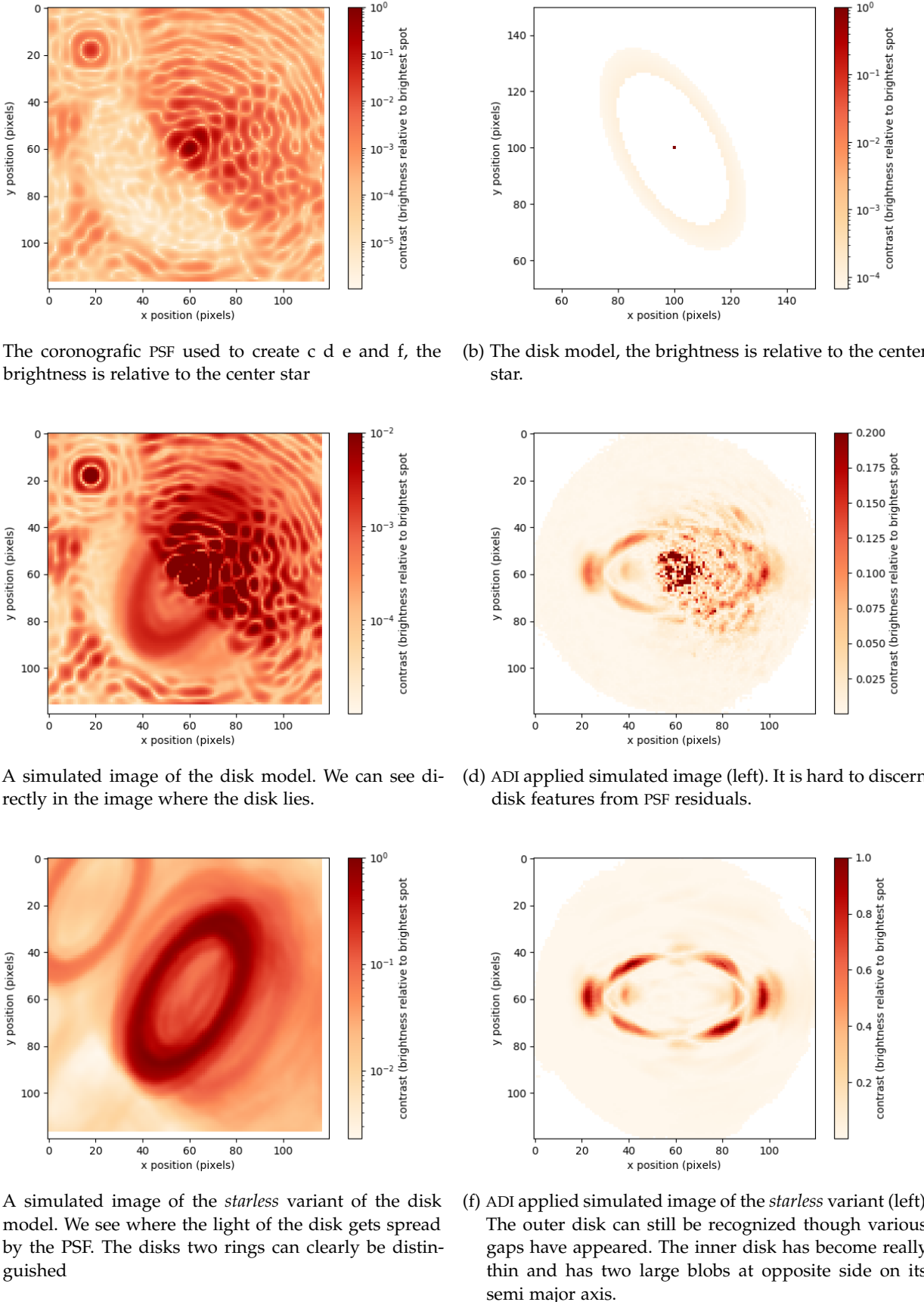


Figure 28: On the top row: the PSF and the disk model used to generate the other images. Then generated images of the disk model en its *starless* variant (left) and results of ADI applied to them (right).

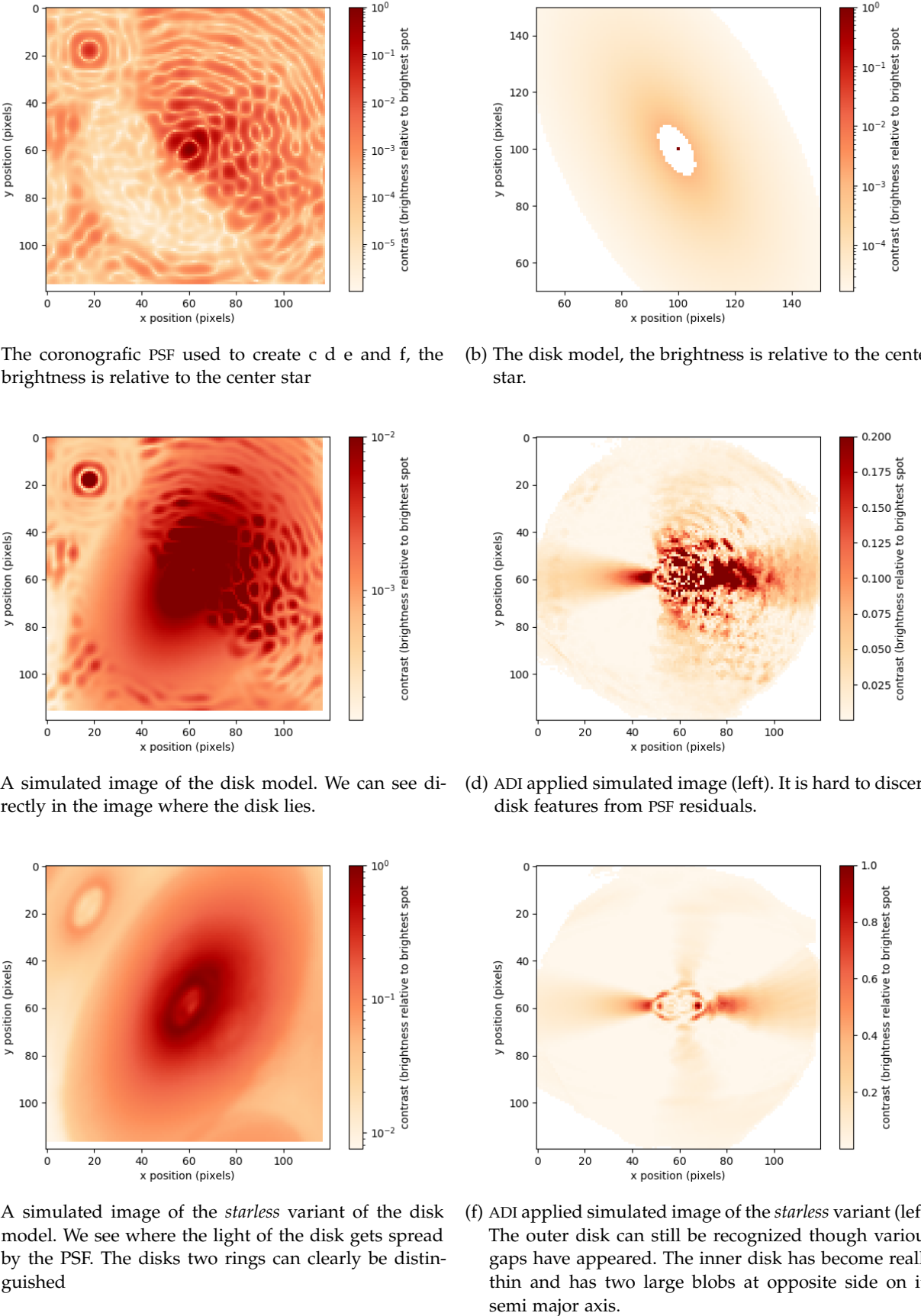


Figure 29: On the top row: the PSF and the disk model used to generate the other images. Then generated images of the disk model en its *starless* variant (left) and results of ADI applied to them (right).

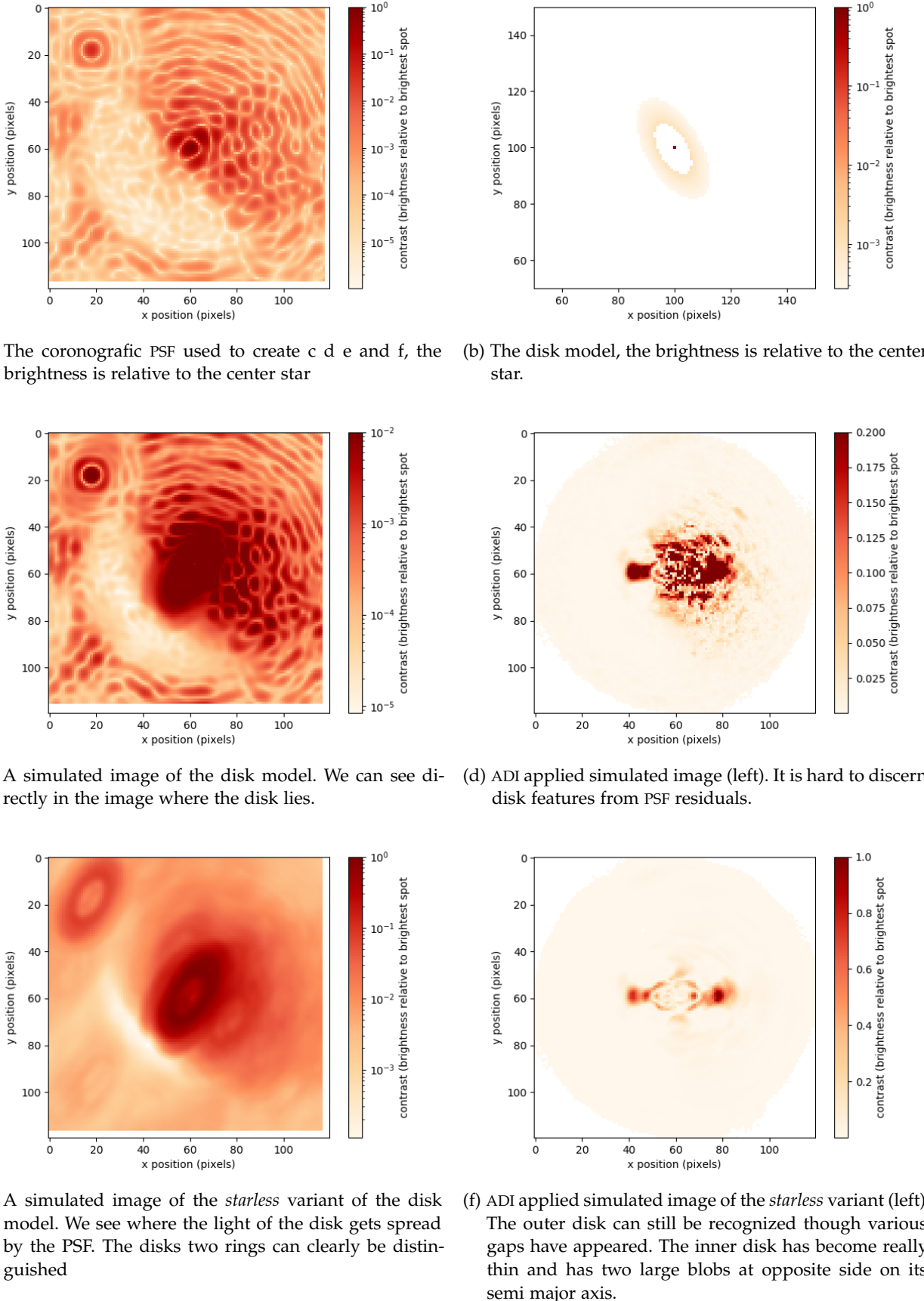


Figure 30: On the top row: the PSF and the disk model used to generate the other images. Then generated images of the disk model en its *starless* variant (left) and results of ADI applied to them (right).

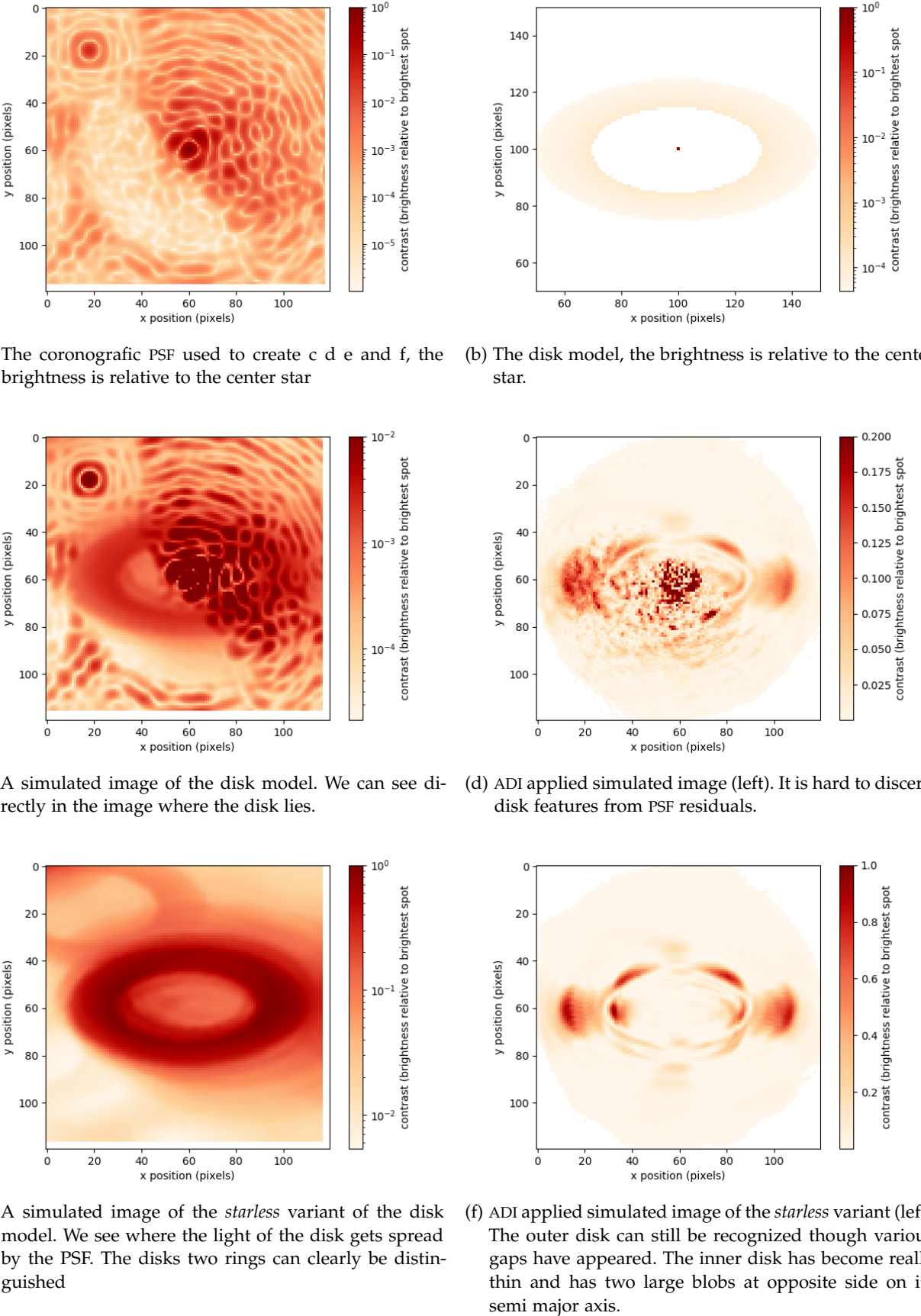


Figure 31: On the top row: the PSF and the disk model used to generate the other images. Then generated images of the disk model en its *starless* variant (left) and results of ADI applied to them (right).

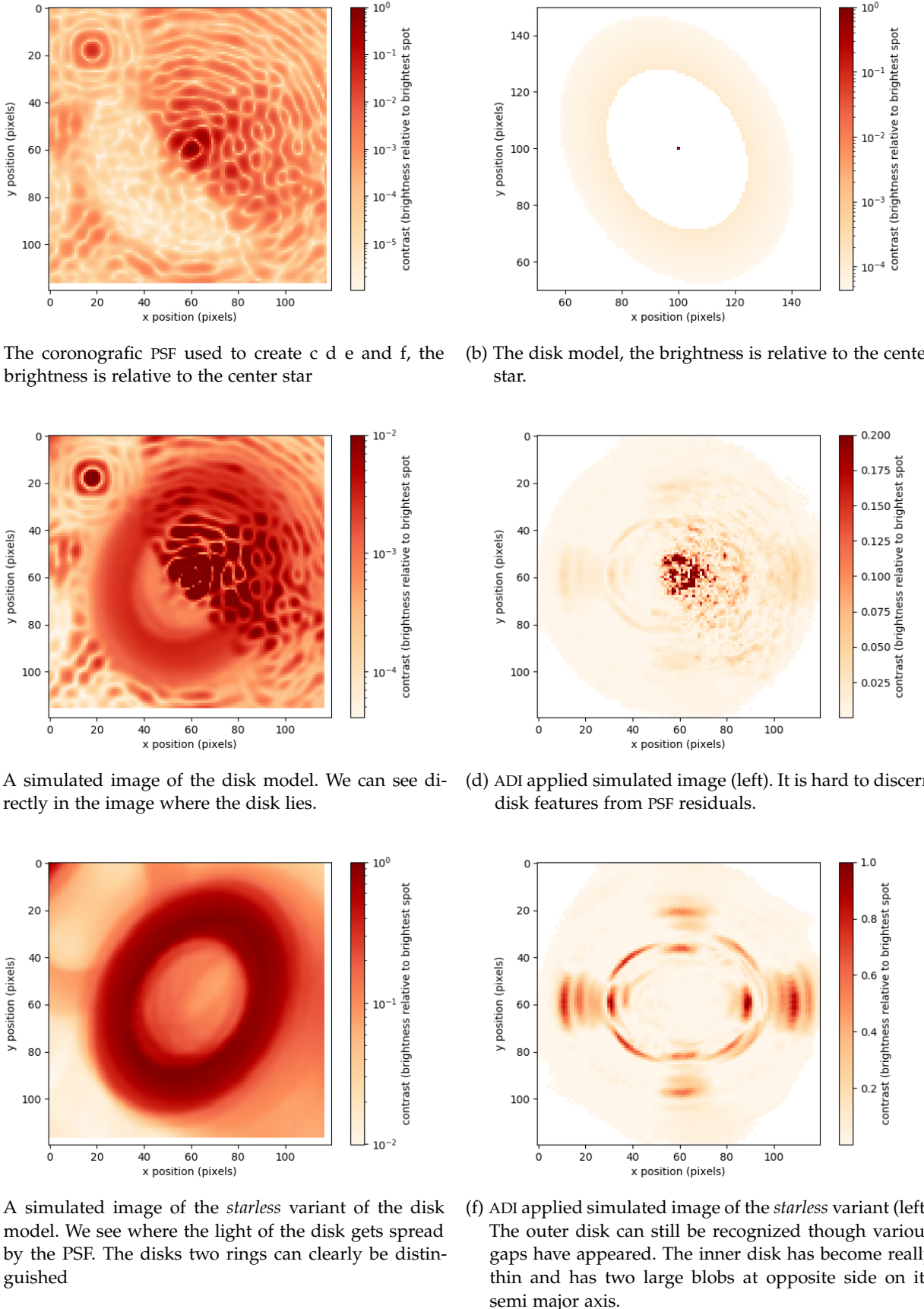


Figure 32: On the top row: the PSF and the disk model used to generate the other images. Then generated images of the disk model en its *starless* variant (left) and results of ADI applied to them (right).